



RESEARCH ARTICLE

10.1029/2020JD033387

Satellite-Derived Characteristics of Saharan Cold Pool Outflows During Boreal Summer

Thomas Caton Harrison¹ , Richard Washington¹, and Sebastian Engelstaedter¹ 

¹Climate Research Laboratory, Oxford University Centre for the Environment, Oxford, UK

Key Points:

- An objective satellite detection and tracking scheme is developed and used to characterize Saharan cold pool outflows across 14 summers
- Cold pool outflows are widespread across the central and western Sahara, peaking in August close to the Mali-Niger-Algeria triple point
- Patterns of cold pool outflow activity can help explain an observed decline in late summer dust emission

Correspondence to:

T. Caton Harrison,
thomas.catonharrison@keble.ox.ac.uk

Citation:

Caton Harrison, T., Washington, R., & Engelstaedter, S. (2021). Satellite-derived characteristics of Saharan cold pool outflows during boreal summer. *Journal of Geophysical Research: Atmospheres*, 126, e2020JD033387. <https://doi.org/10.1029/2020JD033387>

Received 30 JUN 2020

Accepted 9 DEC 2020

Abstract Cold pool outflows (CPOs) are thought to be the most significant meteorological mechanism of mineral dust emission from the world's largest source in the central and western Sahara in boreal summer. An absence of CPOs from numerical models and reanalyses used to simulate Saharan dust emission leads to considerable error in modeling of dust fluxes from the Sahara. As such, the role of CPOs in the observed variability of dust through the monsoon season remains unclear. To remedy these issues, an improved observational benchmark is needed. In this research, an automated approach to identify and track CPOs in dust imagery from the Spinning Enhanced Visible and Infrared Imager (SEVIRI) is derived. The approach is found to flag 74.2% of events identified manually (26/35). 1,559 events are tracked for June, July and August of 2004–2017. CPOs follow a clear diurnal cycle, peaking at 1700–1900 Universal Time Coordinated. Propagation speeds decay exponentially through their lifetime, but on average speeds are 1.5 ms^{-1} higher at night. About 22.5% of the observed events exceed a total traveled distance of 300 km, with an overwhelming preference for northwestwards propagation. Common across the southern central and western Sahara, CPO activity shifts north through summer in line with observed dust emission. The exception to this is the development of an intense hotspot of CPO activity in southern Algeria in August, which does not parallel any known late season outbreaks of dust. The results underline the importance of the southernmost Saharan dust sources, activated by frequent CPO occurrence in early summer.

1. Introduction

The central and western Sahara (CWS) is the world's most active dust-emitting region during boreal summer (Washington et al., 2003). Mineral aerosols play an important role in the Earth's radiation budget on climatic and meteorological timescales, as a source of nutrients and as a pollutant (Boucher et al., 2013). Surface observations and satellite retrievals from the CWS indicate that cold pool outflows (CPOs) from deep convection are the dominant summertime meteorological dust emission mechanism (Allen et al., 2013, 2015; Caton Harrison et al., 2019); Lidar observations from the core of the central Sahara in June 2011 show that two-thirds of emission events detected can be traced to this process (Allen et al., 2013). CPOs responsible for dust emission are often referred to as “haboobs” (Sutton, 1925).

CPOs are the result of mesoscale density currents formed from the latent heat exchange of evaporating precipitation in deep convective downdrafts. Hence, although they are hypothesized to be the dominant dust emission process in the world's largest source region, representation of this process is not surprisingly missing or poor in operational forecasting analyses (Pope et al., 2016; Redl et al., 2016; Sodemann et al., 2015; Trzeciak et al., 2017). They are also mostly unrepresented in coarse resolution global model simulations used for the Coupled Model Intercomparison Project (CMIP) which rely upon convective parameterization (Roberts et al., 2018; Knippertz & Todd, 2012; Marsham et al., 2011), although some attempts have been made to parameterize the role of convective downdrafts (Cakmur et al., 2004; Lunt & Valdes, 2002). Similarly, the resolution of all available reanalysis products, including ERA5 at around 30 km grid spacing (Hersbach & Dee, 2016), is too coarse for inclusion of CPOs. The consequences are stark for dust simulation whether it is embedded in the global models we rely on for climate prediction or derived from offline emission models driven by reanalyses. Exclusion of this key process means that models either emit too little dust or else do so for the wrong reasons (Marsham et al., 2013). Missing CPOs also lead to biases in moisture flux (Garcia-Carreras et al., 2013) which in turn have a large impact upon the simulated top of the atmosphere energy balance in the central Sahara (Marsham et al., 2016).

© 2021. The Authors.

This is an open access article under the terms of the [Creative Commons Attribution License](https://creativecommons.org/licenses/by/4.0/), which permits use, distribution and reproduction in any medium, provided the original work is properly cited.

In the meantime, bespoke numerical model simulations run at convection-permitting scales are able to simulate CPOs (Heinold et al., 2013) with efforts to parameterize the missing processes in mass-flux dependent coarser resolution models (Pantillon et al., 2015). To test these approaches and remedy model deficiencies, an improved observational benchmark is needed. However, direct observations of CPOs are only currently available from extremely sparsely distributed meteorological station data at point locations within the Sahara and Sahel. The characterization of the frequency, diurnal cycle, intensity, and distribution of CPOs across the CWS is critical to evaluating numerical model simulation of dust emission from the world's largest source regions.

1.1. Background

CPOs from mesoscale convective systems (MCSs) propagate often in the summer from the Sahel (Allen et al., 2013; Bou Karam et al., 2008; Flamant et al., 2009; Marsham et al., 2008) and less frequently from the Atlas mountains (Knippertz et al., 2007) into the Sahara, especially during the peak of the West African Monsoon (WAM). CPOs are known also to play a part in sustaining convection as they travel north across the desert, lifting low-level air masses above the considerable summertime convective inhibition (Roberts & Knippertz, 2014; Trzeciak et al., 2017). CPOs appear to be the dominant meteorological mechanism of dust emission, but more attention has been devoted at the intraseasonal timescale to variability in synoptic drivers, including African easterly waves (Cuesta et al., 2009; Grogan & Thorncroft, 2019; Knippertz & Todd, 2010), the Saharan heat low (SHL) (Todd et al., 2013; Ryder et al., 2015), cold surges (Vizy & Cook, 2009) and upper-level dynamics (Knippertz & Fink, 2006; Roberts & Knippertz, 2014). Although these processes are not usually directly responsible for summertime emission, they are sufficiently large to be resolved in the datasets typically used to study them.

Drivers of CPO variability through summer are a subject of debate, as dust emissions appear to peak in June even though this marks only the beginning of the northward migration of the intertropical discontinuity (ITD) low-level convergence band (Engelstaedter & Washington, 2007), with lower dust loadings during the parallel southward retreat in September (Marsham et al., 2008). It has been suggested that dry mid-tropospheric conditions during the early monsoon season could favor CPO development (Marsham et al., 2008), with a small number of observed cases supporting this (Provod et al., 2016). Other possible drivers of this summertime seasonality include suppression of Sahelian dust by rainfall (Bergametti et al., 2016, 2017; Engelstaedter & Washington, 2007), masking of dust in satellite imagery (Heinold et al., 2013; Williams, 2008) and the role of other emission mechanisms such as the nocturnal low-level jet (Allen & Washington, 2014; Fiedler et al., 2013). Recent model-based research shows that the seasonality of dust uplift due to CPOs may differ between the Sahel and Sahara (Pantillon et al., 2016). Observations of cold pool occurrence through summer represent an important missing piece of evidence in this debate.

Observational research into Saharan cold pools makes considerable use of satellite imagery to support detection from in situ observations. This is in part because CPOs do not have a unique signature at the surface (Allen et al., 2013; Hobby et al., 2013), but they do exhibit consistent spatial characteristics in remotely sensed imagery due to an evolving dust arc originating from nearby convective cloud. For instance, Redl et al., (2015) develop an objective scheme for CPO identification by combining in situ surface observations with microwave satellite data. More common is the use of data from the Spinning Enhanced Visible and Infrared Imager (SEVIRI) above the Meteosat Second Generation (MSG) series of satellites. Allen et al. (2013, 2015) identify CPO passage at Bordj-Badji Mokhtar in southern Algeria (within a region of key dust sources) based upon sharp step-changes observed in 10 m wind speeds when they exceed local emission thresholds in conjunction nearby convective cloud detected in SEVIRI data. Imagery from this satellite has also been deployed by Provod et al. (2016) to detect deep convective cloud over Niger, confirm the presence of CPOs and distinguish individual storm clouds from mesoscale convective systems (MCSs). Manual tracking of individual CPO events in SEVIRI has been used to explain the largest dust emission events (Karam et al., 2014; Schepanski et al., 2007) and moisture transport through the Sahara (Flamant et al., 2009; Trzeciak et al., 2017). The 15 min temporal resolution of SEVIRI data makes it well suited for the study of mesoscale dust-emitting processes which operate on a timescale of hours.

In this study, an automated method is derived for the first time to delineate and calculate the propagation speed of outflow boundaries associated with cold pools observable in SEVIRI imagery by virtue of lofted dust at their leading edge. This is used to generate the first data set of cold pool occurrence across dust-emitting regions of the CWS. As dust emission from the Sahara is highly variable from year to year (Mahowald et al., 2010; Prospero & Lamb, 2003; Tegen et al., 2013; Wagner et al., 2016), we use a large SEVIRI data set covering June, July and August of 2004–2017. A previous study (Caton Harrison et al., 2019) made use of the same satellite data set to infer whether observed dust plumes could be linked to CPO activity. Whereas Caton Harrison et al., (2019) aimed to account for all SEVIRI-observed dust, the focus of this paper is a subset of these plumes which can be found at the leading edge of CPO density currents and which therefore render the CPO density current itself visible to satellite. By contrast, a majority of plumes in Caton Harrison et al., (2019) had either no clear outflow boundary or persisted in the atmosphere long after this sharp boundary had dissipated. In summary, this paper aims to:

1. Derive an automated method for identifying and tracking Saharan CPOs in SEVIRI imagery
2. Characterize the diurnal cycle, propagation speed, direction of travel and distribution of CPOs
3. Relate patterns of CPO activity through boreal summer to the seasonality of Saharan dust

Section 2 is devoted to the data and methodology used to detect and track CPOs, with the approach validated in Section 3. A data set of events is presented and linked to dust emission in Section 4.

2. Automated Tracking of Cold Pool Outflow Boundaries

The first step in automated CPO tracking is to identify accurately an advancing haboob from satellite. CPOs achieve their distinctive appearance in SEVIRI false color pink dust composites owing to sharp boundaries induced at their leading edges, with a gradient toward more purple colors in the wake of the outflow boundary as a result of the difference in moisture and dust content between the two air masses (Flamant et al., 2007, 2009). An example of this is shown in Figure 1a. Brightness temperature difference (BTD) fields have been used in the past to pinpoint dust in this type of imagery (Ashpole & Washington, 2012; Bachl et al., 2012; Liu et al., 2012; Murray et al., 2016). One such field is the difference between the 10.8 and 8.7 μm channels; higher emissivity at 8.7 μm highlights regions of dust and rocky desert surfaces (Banks et al., 2018), the latter of which may be subtracted by calculating a BTD anomaly field relative to a 15 days moving window (Figure 1b) as in Ashpole and Washington (2012). It follows that the regions of the image undergoing the most rapid changes in BTD are the most likely to be situated in regions of sharp environmental change such as the abrupt gradients at the leading edge of passing density currents. It is important to note that the methodology in this paper is not geared toward observing and tracking all dust plumes as in Ashpole and Washington (2013b) or Caton Harrison et al. (2019). Instead, we focus specifically upon the leading edge of CPOs which are uniquely observable in the CWS thanks to an abundance of erodible material. Hence, our aim is to extract information about the density currents marked by dust rather than all dust plumes identifiable in SEVIRI.

Figure 2 provides an overview of the detection scheme adopted in this paper. The algorithm operates in two overarching phases. In the first phase, imagery is processed to extract the 10.8–8.7 μm anomaly field, a persistence-based temporal gradient is applied and a mask is used to delineate candidate CPO features. In the second phase, these features are tracked as objects; those with a low duration and peak size are discarded, as well as events with no association with deep convection or to any dust pixels.

2.1. Algorithm Phase 1: Candidate CPO Masking

A first step is to identify regions with rapidly changing BTD. To achieve this, the sum of the differences between the BTD anomaly of the image being analyzed and each of the previous four images (i.e. one hour) is taken. The use of a sum over four images identifies pixels at which a brightness temperature gradient is not only induced but also maintained. This in turn helps to distinguish between frontal (CPO) features that induce a sustained change in environmental conditions and more temporary cloud passages. The gradient of BTD calculated over four 15 min intervals (one hour) is referred to henceforth as the BTD Gradient

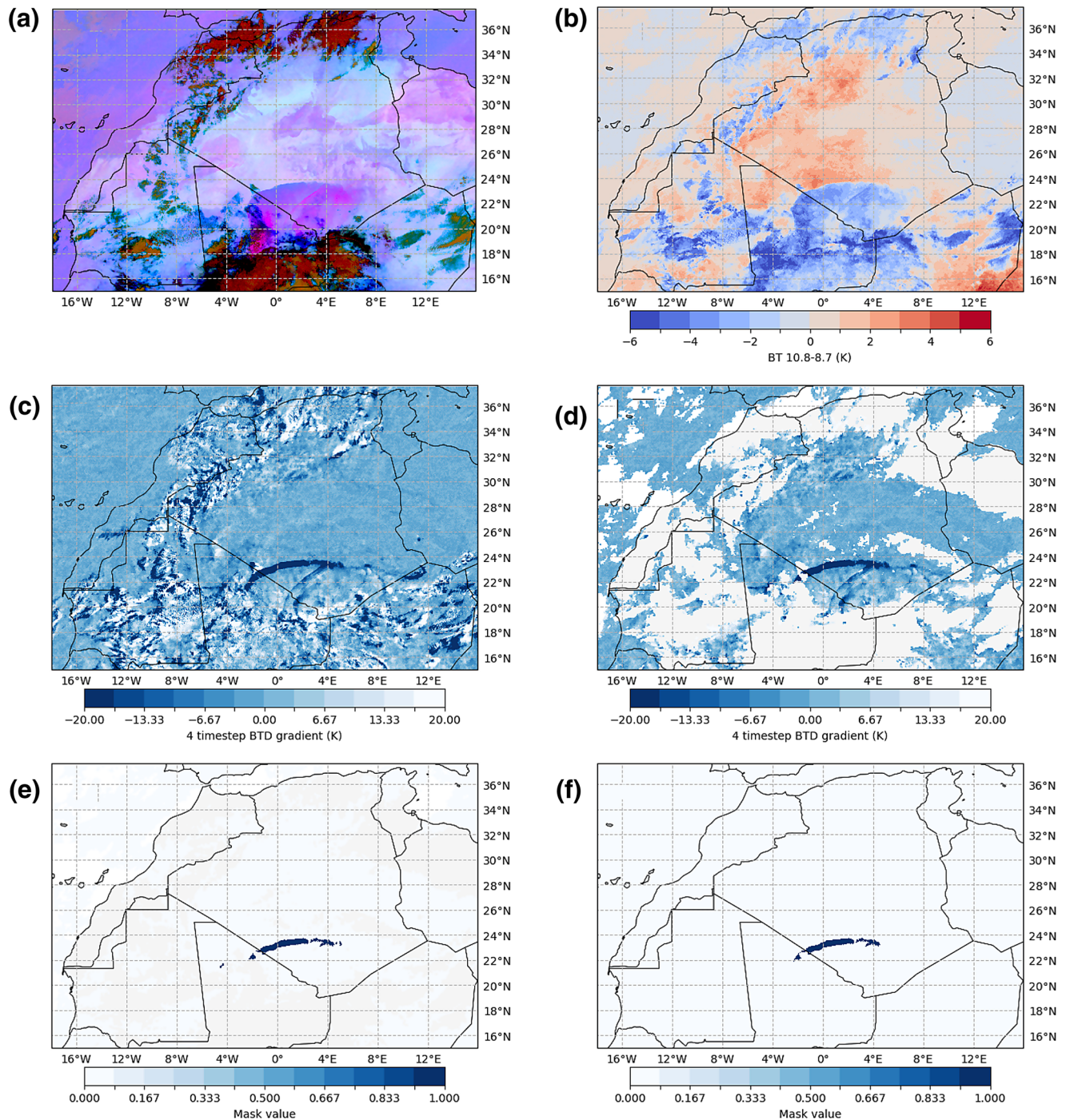


Figure 1. (a) Original SEVIRI pink dust composite from 0115 UTC 10th of July 2011. (b) Difference (K) between the 10.8 and 8.7 μm brightness temperature channels, taken as an anomaly relative to a 15 days moving window. (c) The sum of the difference between the field shown in (b) and the same field for the previous three timesteps. (d) Cloud masking applied. (e) Only regions where the values of (c) are under -20 K and contain at least one pixel with a value under -30 K (with a total pixel cluster size over 20). (f) Final tracked CPO after events not meeting the tracking conditions (red boxes in Figure 2) are discarded. CPO, cold pool outflow; SEVIRI, Spinning Enhanced Visible and Infrared Imager; UTC, Universal Time Coordinated.

(BTDG). The CPO boundary is clearly defined at this point (Figure 1c), but also a myriad of other features at the edges of prominent clouds.

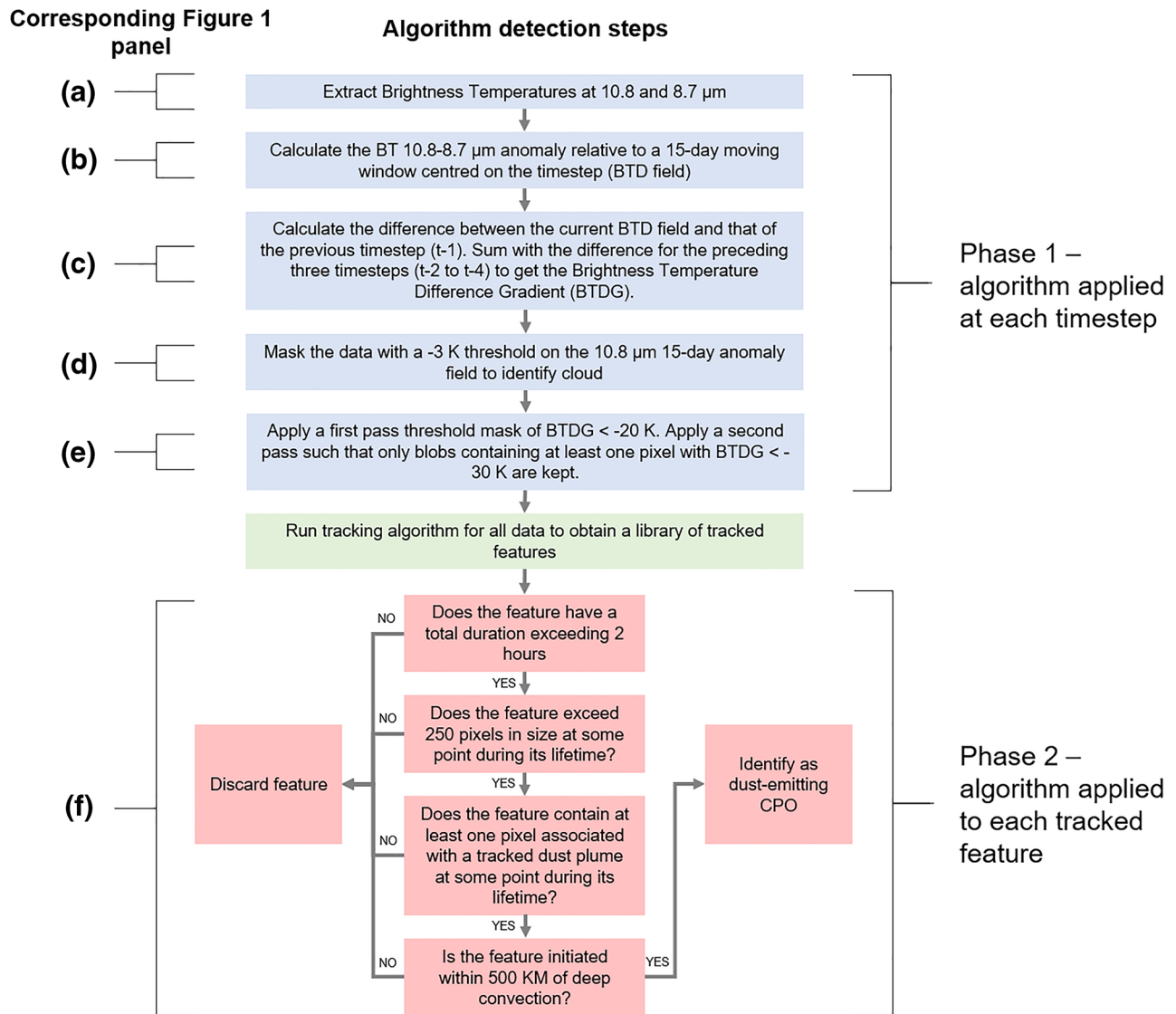


Figure 2. Flow chart showing steps involved in the CPO detection algorithm. Boxes shaded in blue represent the initial detection phase applied to each timestep of raw SEVIRI data, corresponding to panels in Figure 1. The output from this is run through the tracking algorithm (green box) and conditions are applied to the tracked features to determine which events are retained or discarded (red boxes). CPO, cold pool outflow; SEVIRI, Spinning Enhanced Visible and Infrared Imager.

Clouds are identified and subtracted in this paper as in Ashpole and Washington (2012), using the BT 10.8 μm channel. In order to bypass the effect of varied cloud top radiance through the day upon masking, the anomaly of the 10.8 μm channel relative to a 15 days moving window average for the given time of day is taken, as for BTDs. Pixels with a BT 10.8 μm anomaly of -3 K are masked as cloud (Figure 1d). The EUMETSAT cloud mask product was also tested, but not used as it falsely identifies lofted dust as cloud, masking a large number of CPO events.

To identify and delineate unique objects, a threshold-based mask is applied to the BTDG field which categorizes each pixel within the scene for a given timestep as “CPO” or “No CPO.” Unlike in a model-based approach (Heinold et al., 2013; Pantillon et al., 2016), there is no physical basis for selecting a particular value of BTDG as the threshold, so an empirical approach is adopted to applying the correct mask.

To test for an optimal threshold to apply to the imagery, a training period is used. A very generous starting threshold of $\text{BTDG} \leq -10$ K was applied to all data from July 2010, and the resultant features were tracked.

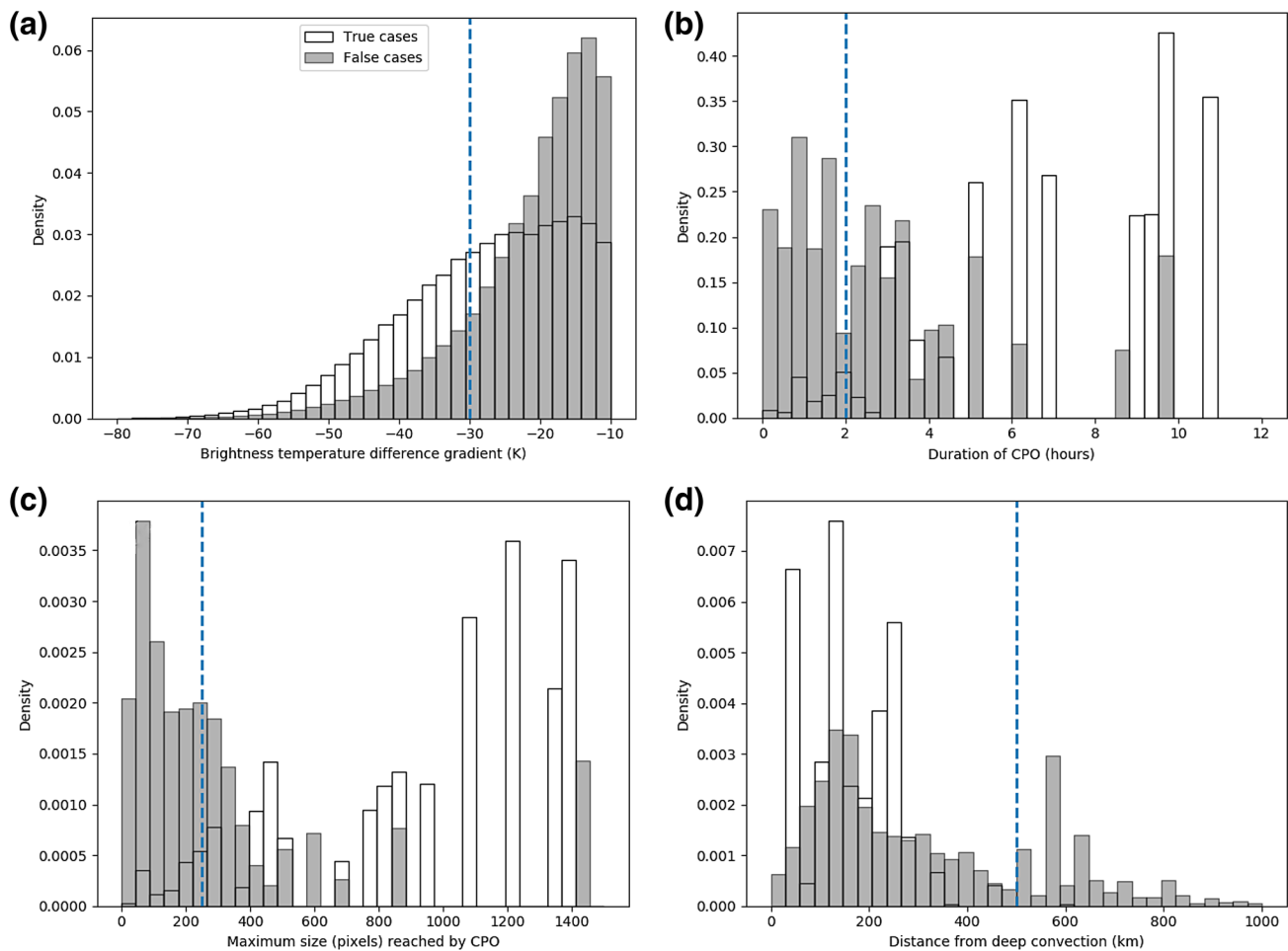


Figure 3. Probability density functions of (a) brightness temperature difference gradient (k), (b) CPO duration (hours), (c) maximum pixel size reached by events during their lifetime and (d) distance from deep convection for true (white) and false (dark gray) events tracked manually through July 2010. Each pixel of an event (true or false) counts as one sample in the distribution. Blue dashed vertical lines indicate the thresholds chosen for the CPO detection algorithm. CPO, cold pool outflow.

Each of the 2,976 images for the month was analyzed manually to identify genuine CPO features according to the following conditions:

1. The feature is not an artifact from the presence of cloud
2. Deep convective cloud is present upstream of the feature (within approximately 500 km)
3. A sharp frontal boundary in lofted dust and low-level moisture is present
4. The feature was recently generated (i.e., not an aged dust plume with a sharp edge)

The corresponding automatically tracked features from the training data set were then identified. All events generated for the training data set which did not fulfill the conditions described above were classified as false alarms. BTDG values for both true and false events were then compared to determine an appropriate threshold to distinguish the two.

A distinction between genuine and false alarm CPOs becomes clear below a BTDG around -30 K (Figure 3a). This value is selected as the basic threshold for CPO detection. Two issues remain, however: first, a large number of true CPOs have BTDG values above -30 K. Second, false alarms are still common even below -30 K. To address the first issue, a “second pass” threshold of $\text{BTDG} \leq -20$ K is applied, which allows all pixels passing this threshold to be accepted as long as they are connected to an existing feature of

BT_{DG} ≤ −30 K values. With these two masks applied, the clear CPO in Figure 1e is successfully delineated. To address the second issue, however, an additional set of identification criteria is needed.

2.2. Algorithm Phase 2: Discarding False Positive Tracked CPOs

In order to further reduce false alarms (for example seen in Figure 1e near 22°N, 4°W), events are discarded according to characteristics calculated across their entire lifetime. Genuine events are commonly found to exhibit much longer durations (Figure 3b), whereas false events cluster under the 2 h mark and none exceed 10 h. We therefore apply a minimum duration of 2 h to the detection scheme. 3.6% of true pixels and 42.5% of false pixels are below this threshold. A second factor is the maximum size individual events reach during their lifetime, as measured by the number of pixels belonging to a feature. Most true CPOs exceed 250 pixels at some point during their lifetime (Figure 3c), so this is also used as a cutoff. About 6.6% of true pixels and 60.7% of false pixels are below this threshold. Third, CPOs whose centroids were more than 500 km from deep convection (identified here where BT 10.8 μm has a value less than 250 K) at the point of generation are excluded (Figure 3d). For this criterion, only 0.4% of true pixels are above the 500 km threshold, whereas 30.2% of false pixels are. Finally, CPOs may only be detected if they are also associated with a dust-flagged (following Ashpole & Washington, 2012) pixel at some point in their lifetime. This final condition reduces the hit rate from 82% to 80% but crucially decreases the false alarm rate from 13.8% to 5.2%. The result of these conditions in the case of Figure 1f is an isolated CPO feature.

A value of 250 K is on the warm end of thresholds for detection of convective cloud, especially when looking for mature systems for which 215–225 K may be used (Bedka & Khlopenkov, 2016; Bedka et al., 2010). Table 1 in Bain et al. (2010) gives a range of IR thresholds used for detection of convective cloud. Warmer thresholds have been used to detect deep convection over West Africa, including 270 K in Lavaysse et al. (2009) and Ashpole and Washington (2012). 270 K was tested but found to be too generous, flagging regions of thin cirrus and thick mid-level clouds. On the other hand, stricter thresholds such as 230 K were too stringent, flagging only the deepest systems and missing warmer cloud tops near developing CPOs.

Several caveats limit the usage of this algorithm. First, at a fundamental level, the method relies upon the appearance of clear boundaries in low-level dust indicating the presence of a cold pool outflow boundary. Hence, as with all dust detection (Brindley et al., 2012), an atmosphere with high column water vapor already is likely to obscure outflow boundaries. Second, as with many other forms of remote sensing, cloud cover is also a factor which hinders observation. For the purposes of this paper, this means that only the strongest CPOs which become spatially separate from their generative convection are observed. The algorithm as a whole is constrained by the need to minimize false alarms, hence it is not suited for detection of small, brief (<2 h) events and misses weaker events which could be detected manually. The accuracy of the algorithm is quantified further in Section 3. Nevertheless, the major strength of this automated approach is its capacity to cover a long period of data with an entirely reproducible approach.

2.3. Estimating Propagation Speed and Direction

One of the defining features of an outflow boundary observed from space is its organization along a semi-ellipse-like axis elongated perpendicular to its direction of propagation (Caton Harrison et al., 2019). Detected outflow boundaries are expected to adhere to a certain shape throughout their lifetime, consisting of radial expansion away from convective cloud with a clearly defined leading edge. Radial spreading of downdraft mass has been used as a conceptual framework for parameterized CPOs in the Met Office Unified Model (Pantillon et al., 2015). Seen from the top down without vertical information, an even simpler approach can be used to track the speed of satellite-observed CPOs.

Speed-tracking is achieved here by fitting CPOs identified with the technique in Sections 2.1 and 2.2 to a simple 2D top-down model of an idealized propagating outflow boundary (Figure 4). In this model, the direction of the CPO is perpendicular to its orientation and the speed is calculated by taking the distance between the leading edge of detected features at consecutive 15 min timesteps.

This approach is simplistic and assumes background winds do not significantly modify the direction of CPO travel. However, its main advantage is that it overcomes the issue of variable signal strength when detecting features from satellite. At the beginning of an event's lifetime (shown as t_0 in Figure 4), only a small proportion of the event's true size is visible to a satellite. This is in part because the BTDG gradient has not reached its peak yet when measured across several timesteps, but also because cloud obscures the signal as the CPO emerges from below. Furthermore, toward the end of the CPO's lifetime (shown as t_4 in Figure 4), the feature's total area tends to diminish as the signal weakens. Hence, if the more flexible approach of tracking feature centroids (marked as blue crosses in Figure 4) had been used in isolation, the position of the CPO through time would have been observed to evolve erratically as parts of the CPO became obscured.

Two key ingredients are needed to calculate propagation speed from this model. First, a direction of propagation is needed in order to identify the leading edge of the CPO. Second, displacement vectors are needed between consecutive leading edges. As this model assumes that CPOs propagate in a direction perpendicular to their orientation, the direction of travel can be obtained from the orientation of a CPO. This orientation is in turn calculated from the timestep with the largest number of detected pixels, comprising the most complete view of the CPO (highlighted in white in Figure 5).

The pixels which are furthest along the axis of the approximated direction of travel are assigned as the leading edge of the CPO, shown as red dots in Figures 4 and 5. Finally, leading edge pixels are matched between consecutive timesteps to obtain displacement vectors (shown as black arrows in Figures 4 and 5); pixels are matched if they are nearest neighbors and if the angle between them does not differ from the CPO propagation direction by more than 30° . A displacement vector is only calculated when a pixel has a match. The final speed value for a given timestep is calculated from the mean of all displacement vectors for that timestep. CPOs which appear to regularly switch direction are discarded as unreliable, here defined as events for which under 90% of timesteps have a centroid direction within 30° of the CPO propagation direction calculated from its orientation.

This rigid 2D model fitting approach is effective for estimating propagation speeds as many samples are collected for each CPO event; CPOs may be traveling at a slightly different speed in different regions along its leading edge (for instance due to surface roughness), but as samples are taken across its entire width the final mean value is representative. Furthermore, it is robust to periods in the CPO lifetime when detection is poor as it assumes a fixed direction and orientation.

3. Validation

Cold pool outflow boundaries detected automatically by the algorithm developed in Section 2 are intended to map onto those identified by the manual observer. We adopt two validation criteria:

1. Consistency with manual observations from SEVIRI
2. A clear signal in surface observations

As the parameters of the detection algorithm were tuned to data obtained from July 2010, a separate period (July 2011) is used to validate the method and determine its accuracy for criterion 1.

Examples of the algorithm masking pink dust imagery (Figure 6) show that outflow boundaries are successfully detected in proximity to deep convection in the Sahel and Sahara, typically with dust trailing behind. Some curvature of the feature is evident in each case. In some instances (Figures 6c and 6e), parts of the outflow boundary are either masked by arcus cloud or the gradient at the leading edge is too low. The algorithm appears to be capable of distinguishing between genuine outflow boundaries and the edges of cloud features, aged dust or nocturnal low-level jet dust.

35 events in total were identified manually from July 2011, with 26 identified by the automated scheme, indicating a 74.2% hit rate. Only 6.8% of the total pixels flagged by the automated CPO tracking scheme could not be assigned to a genuine event visible to the manual observer. Hence, although certain events are missed the false alarm rate is low.

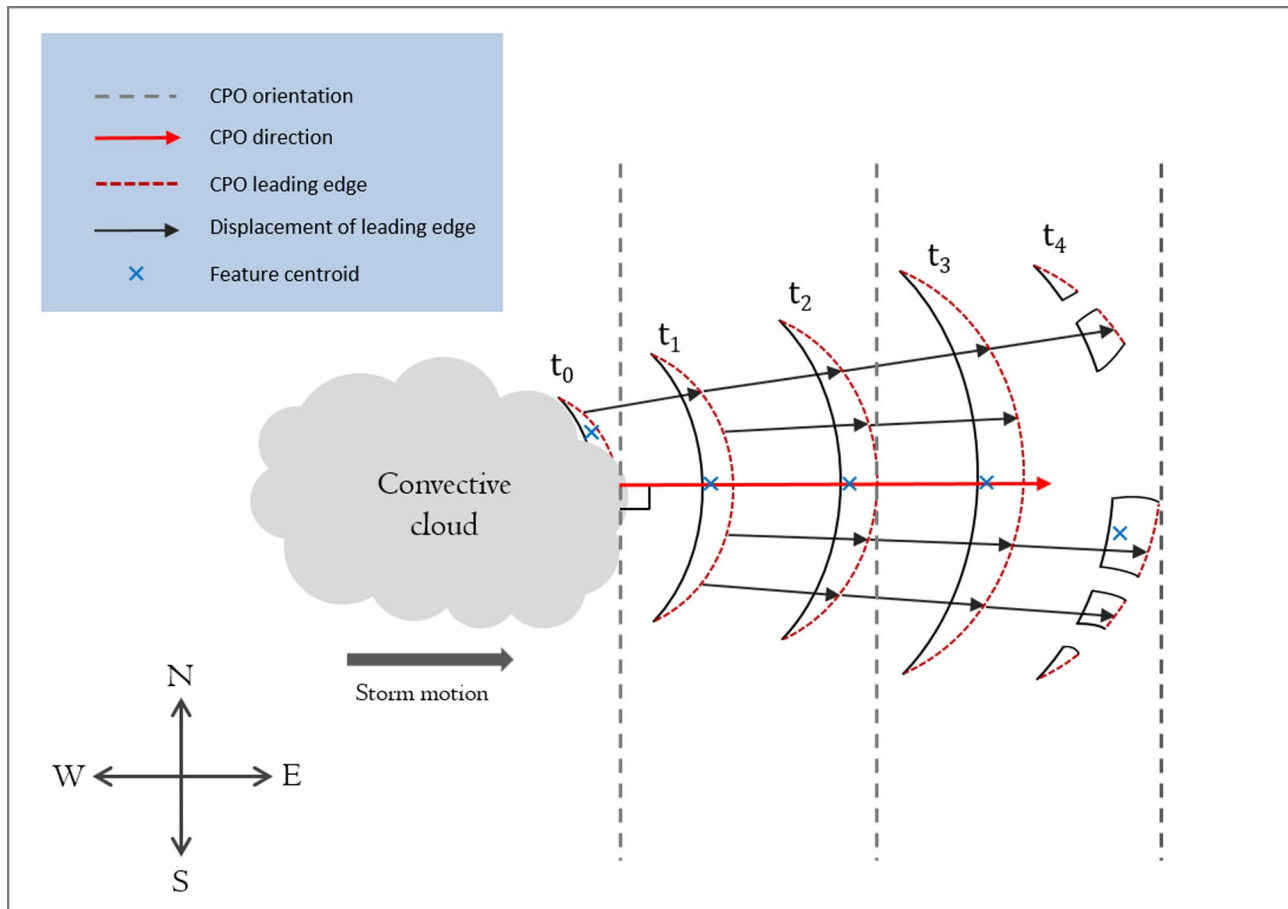


Figure 4. Top-down (bird's eye view) 2D model of a CPO event observed by satellite. Arcs propagating eastwards from a convective cloud represent the progress through time of the outflow boundary. The orientation of the CPO (dashed gray vertical lines) is fixed, and its direction (red horizontal arrow) is perpendicular to its orientation. Red dotted lines represent the leading edge of the advancing outflow boundary while black solid lines represent the trailing edge. Black arrows represent the displacement of this leading edge from t_{n-1} to t_n . The event is first observable at t_0 , (although obscured by cloud) and last observable at t_4 (although the feature has disintegrated into separate entities). Blue crosses indicate the feature centroid. CPO, cold pool outflow.

To address criterion 2, a comparison between Fennec automatic weather stations (AWS) (Hobby et al., 2013) and automatically identified CPOs is made and provides strong evidence that events identified with this method correspond to phenomena observable at ground level. Here, days within the AWS data set for 2011 and 2012 are flagged where an automatically identified CPO boundary passes within 1 decimal degree of latitude or longitude (about 111 km) of the station. Each individual case is then reviewed with manual analysis of SEVIRI imagery to check that the outflow boundary did indeed pass over the station.

Meteorological variables used to detect the passage of a CPO from AWS data include sharp changes in wind direction, pressure, gustiness and temperature (Emmel et al., 2010; Engerer et al., 2008; Provod et al., 2016) as well as dewpoint temperature and mean wind speed (Allen et al., 2013; Redl et al., 2015). However, observations from the CWS show that passing CPOs do not always induce temperature, moisture or pressure changes but that wind speed jumps of at least 3 ms are a robust criterion (Allen et al., 2015). By this metric, of the 23 SEVIRI-detected CPO events occurring near the AWS network, 17 exhibit a signal within the AWS data. A selection of examples is shown in Figure 7. Although a response in both wind speed and humidity is present in almost every case, the magnitude and rapidity of the change induced varies considerably, with some events (e.g., Figures 7a and 7b) exhibiting small jumps in humidity in spite of large changes in wind speed, while others (e.g., Figures 7d and 7g) exhibit large jumps in both variables.

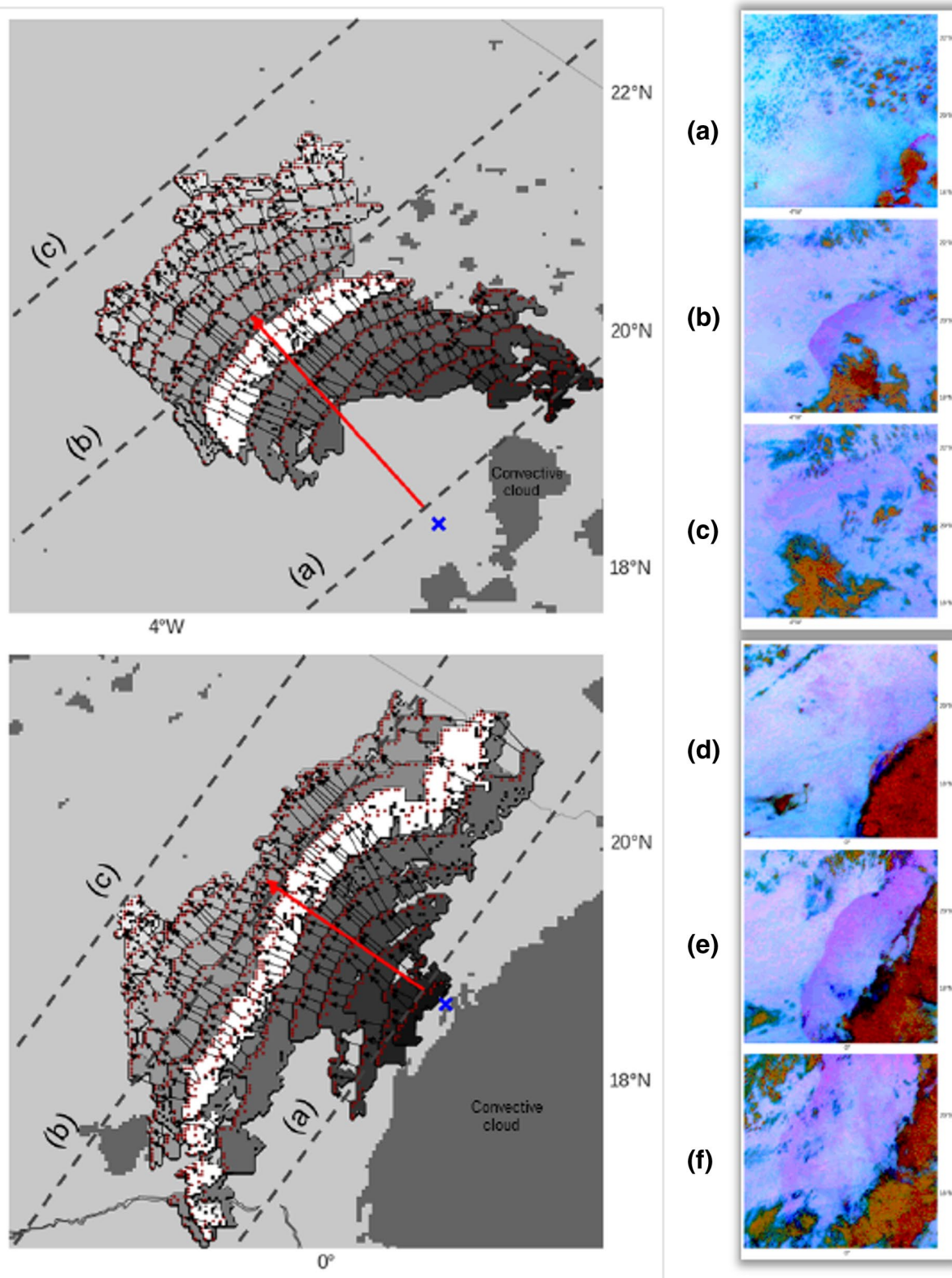


Figure 5. Results of algorithm used to calculate CPO propagation speeds, demonstrated for two CPOs lasting 8 h and 30 min from 15:30 on 09/07/2010 (upper) and 6 h and 30 min from 18:30 on 28/07/2004 (lower), with pink dust imagery shown for (a) the first timestep, (b) the timestep with the most pixels and (c) the final timestep. Every second timestep of the CPO's lifetime is overlain, from the earliest (darkest grays) to the latest (lightest grays). The timestep corresponding to (b) is shaded in white. Dashed gray lines show the orientation of this timestep, from which the CPO direction (red arrow) was calculated. Also shown is the leading edge of each timestep (red pixels) used to obtain propagation speeds (vectors marked as black arrows). A blue cross is marked as an estimate of the origin of the CPO, used for CPO composites in Figure 9. CPO, cold pool outflow.

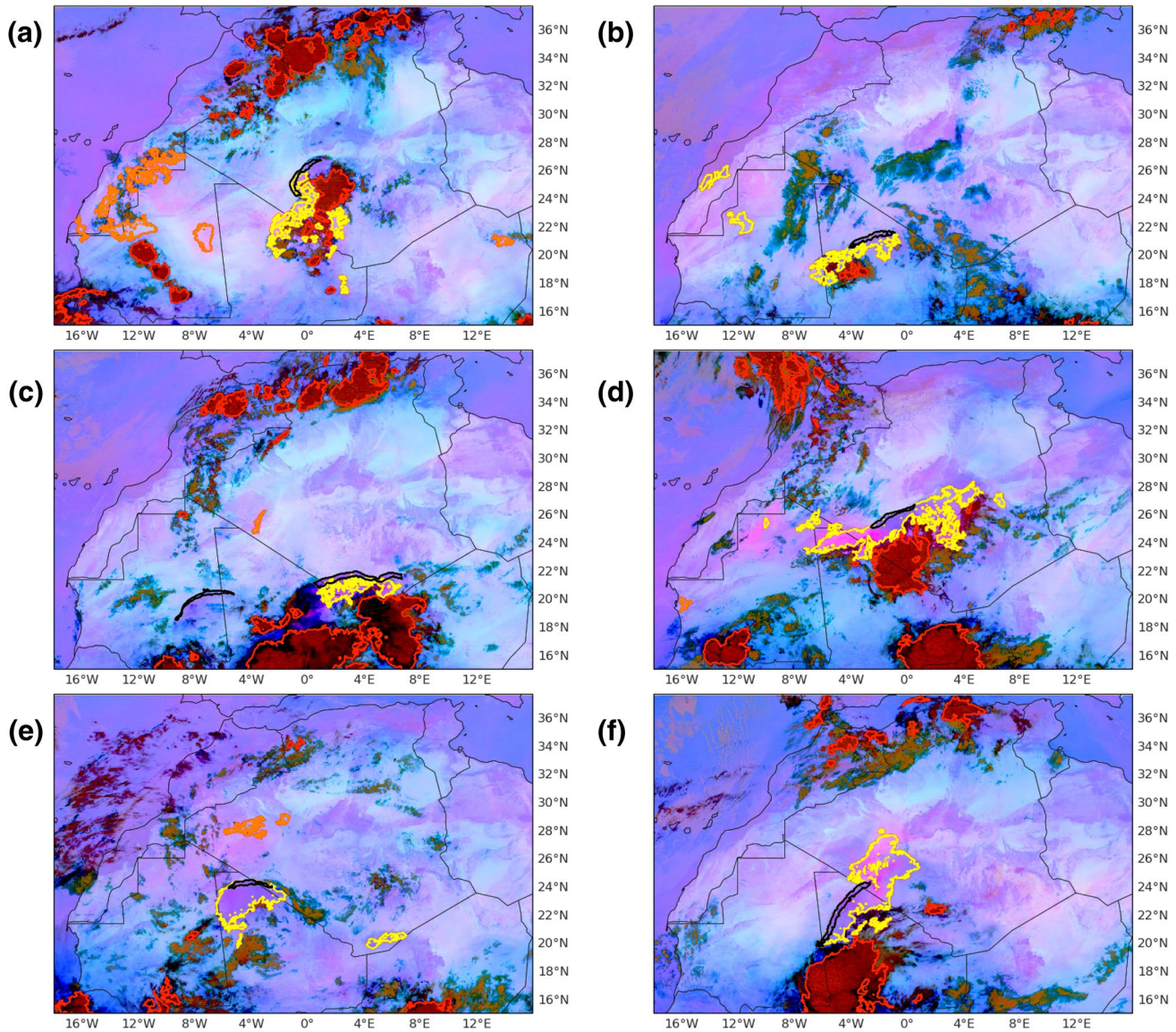


Figure 6. Examples from 2011 of automatically detected CPO outflow boundaries relative to other dust and deep convective cloud features in SEVIRI pink dust imagery. Contoured features include outflow boundaries (black), deep convective cloud (red), dust emitted due to CPO activity (yellow) and dust emitted due to nocturnal low-level jet activity (orange), distinguished with the method described in Caton Harrison et al. (2019). Times shown include (a) 20:00 UTC on 21/06/2011, (b) 01:00 UTC on 05/07/2011, (c) 20:45 UTC on 09/07/2011, (d) 04:45 UTC on 01/08/2011, (e) 04:00 UTC on 09/08/2011 and (f) 05:15 UTC on 29/08/2011. CPO, cold pool outflow; SEVIRI, Spinning Enhanced Visible and Infrared Imager; UTC, Universal Time Coordinated.

Although this algorithm is effective at identifying the leading edges of dust-laden CPOs in SEVIRI, it is important to emphasize that it relies upon the presence of erodible material for a visual signature and cannot account for CPOs entirely hidden under cloud. The data set presented here is therefore a sample of the total population of CPOs and is more suitable for observing long-lived events associated with multicellular convection rather than those caused by microbursts which may only be brief (Roberts & Knippertz, 2012). A complete climatology of CPOs would require a dense surface observation network capable of tracking CPO passage from ground-level where cloud cover is present. Nevertheless, CPOs are regularly visible to satellite and this algorithm detects the majority of them (74.2%). The resulting data set is accurate enough to be meaningful and large enough to calculate long-term statistics.

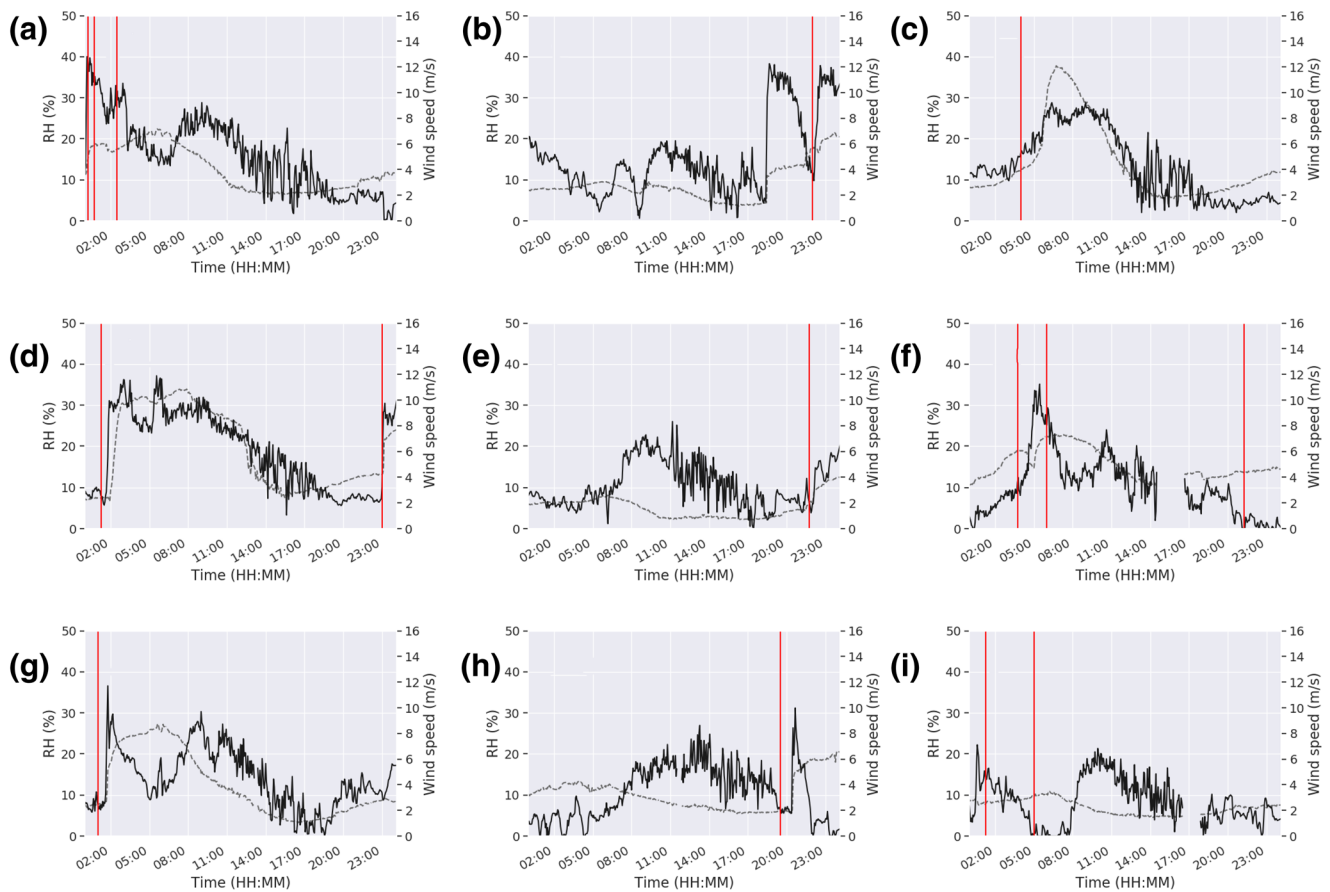


Figure 7. Examples of passages of automatically detected cold pool outflow boundaries compared with contemporaneous measurements of surface wind speed (solid black line) and relative humidity (dashed gray line) from the Fennec automatic weather station network. The closest passage of the detected cold pool outflow is marked with a vertical red line. Events shown are those observed at AWS 134 and 138 as these had the most complete set of measurements, including (a) 21/06/2011 (138), (b) 21/06/2011 (134), (c) 05/07/2011 (134), (d) 10/07/2011 (134), (e) 14/07/2011 (134), (f) 23/06/2012 (138), (g) 27/06/2012 (134), (h) 05/07/2012 (138) and (i) 26/07/2012 (138). AWS, automatic weather station.

4. Results and Discussion

4.1. Characteristics of Tracked CPOs

1,559 events are tracked for the period June, July and August 2004–2017, comprising an average of 111.4 ± 27.0 (one standard deviation) events detected per summer season in the CWS.

A clear diurnal cycle of CPO occurrence is observed (Figure 8a), with peak time for generation of CPOs between 1700 and 1900 Universal Time Coordinated (UTC). This peak likely lags the true outflow production time as the algorithm developed in Section 2 depends upon the leading edge of the CPO emerging from beneath convective cloud as it begins to spread horizontally. The diurnal cycle presented here confirms that the significance of nocturnal dust emission (Allen et al., 2013; Marsham et al., 2013; Todd & Cavazos-Guerra, 2016) is a result of the sharp peak in cold pool generation in the evening as convective systems mature, corresponding also to the peak in convective cloud (Figure 8b) and approximate peak rainfall time observed in TRMM data (Hirose et al., 2008). The results also suggest that this peak in nocturnal dust emission is likely to occur before midnight.

With no ambient flow and a constant mass flux feeding the expanding outflow, the outflow boundary propagation speed U is expected to decay through its lifetime with the form

$$U \propto (t - t_0)^{-\frac{1}{4}} \quad (1)$$

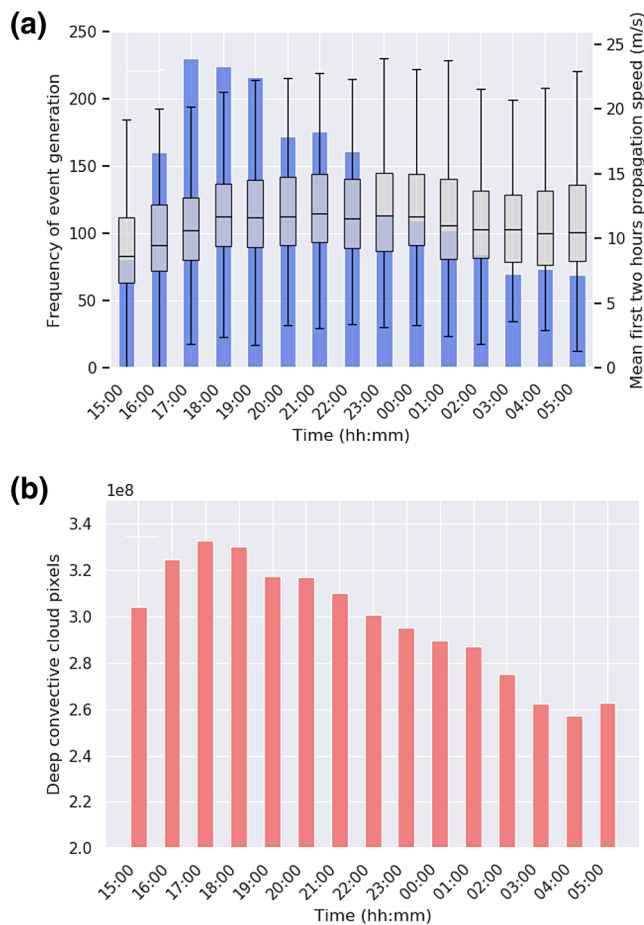


Figure 8. Mean diurnal cycle of (a) CPO generation, taken as the first timestep of detection (blue bars), CPO propagation speed over the first 2 hours (box plots). Shown in (b) is the diurnal cycle of deep convective pixels (where $BT\ 10.8\ \mu m < 250\ K$). All diurnal cycles are calculated for the period June, July and August 2004–2017. CPO, cold pool outflow.

Following Parker (1996), where t_0 represents the time at which the cold pool was generated. Neither assumption inherent in this model is entirely appropriate for the features observed here; ambient flow is present and mass flux depends upon the lifetime of the convection from which the cold pool originates. Furthermore, t_0 cannot be accurately quantified as cold pools are not visible to satellite at the point of inception. Nevertheless, we note that mean propagation speed evolution in Figure 9a conforms well to exponential decay, with event speed greatest closest to the initiation point of the CPO (Figure 9d). The decline in speeds is greatest during the first 2 hours of a CPO's lifetime, in which speeds drop by $2\text{--}2.5\ \text{ms}^{-1}$, falling by a further $2.5\ \text{ms}^{-1}$ over the next 6–7 h.

When composited, an extremely dominant signal of north-northwestwards propagation is found, with a small signal from events propagating toward the southwest (Figure 9b). The events with the greatest duration and reach (over 9 h and 500 km, respectively) are northwestwards. The detection algorithm adopted here depends upon lofting of dust at the outflow boundary. Dust emission is, in turn, nonlinearly related to horizontal wind speeds (Bagnold, 1941). However, simulated cold pool outflows exhibit asymmetrical horizontal wind speeds across their radius; wind speeds realized at the point of cold pool passage are a function of both the radial velocity of the outflow and the “steering” wind aloft from which momentum is transported during the downdraft process (Holmes & Oliver, 2000; Pantillon et al., 2015; Parker, 1996). Hence, upper-level flow opposing the propagation direction of the outflow will slow its progress and reduce the low-level wind speeds responsible for dust emission. These observations support this model of cold pool development; a combination of high dust availability to the north and an easterly steering jet aloft during summer (Thorncroft & Blackburn, 1999) results in a dominant northwestward outflow propagation direction. Cold pools are less prone to propagate along the axis of the dominant summertime southwesterly low-level flow (D. Parker et al., 2005). 22.5% of CPOs (351 events) exceed 300 km in reach in the data set (Figure 9b), demonstrating that over the 14 year period (1,288 days), far-reaching events are relatively common.

Propagation speed also exhibits a slight diurnal cycle (Figure 8a). To remove the effects of the speed decay upon this diurnal cycle (considerably more events are initiated at 1900 UTC than 0800 UTC so average speeds would naturally be higher as per Figures 9a) a mean value has been calculated from the first two hours of speeds (i.e. eight samples). CPO speeds reach a peak at 2100 UTC, several hours after the 1900 UTC maximum in CPO occurrence. Speeds for most daytime hours are not shown, as a manual check of the small sample size of these rare daytime CPOs indicates that more than half are false positives (not shown). Speeds for the hours of 1500–1700 UTC average at $10.7\ \text{ms}^{-1}$, compared with $12.3\ \text{ms}^{-1}$ for all other shown hours. Lower propagation speeds during the daytime demonstrate the effect of boundary layer mixing; eddy-driven turbulence in the daytime convective boundary layer inhibits horizontal transport (D. Parker et al., 2005).

4.2. Seasonality of CPOs and Comparison with Dust Emission

CPO activity is nonuniform across the CWS (Figure 10). The vast majority of detections are found south of 28°N and propagate northwestwards, indicating the major CPO generation mechanism is deep convective activity associated with the WAM. The peak in CPO activity occurs close to the Mali-Niger-Algeria triple point (TP) at $4^\circ\text{E}, 20^\circ\text{N}$. This CPO maximum is proximate to a hotspot of orographic deep convection (Redl et al., 2015), known to be a likely driver of enhanced cold pool activity (Kocha et al., 2013). Other hotspots of activity are found along the western flank of the Adrar des Ifoghas mountains ($4^\circ\text{--}0^\circ\text{W}, 20^\circ\text{N}$) and to the

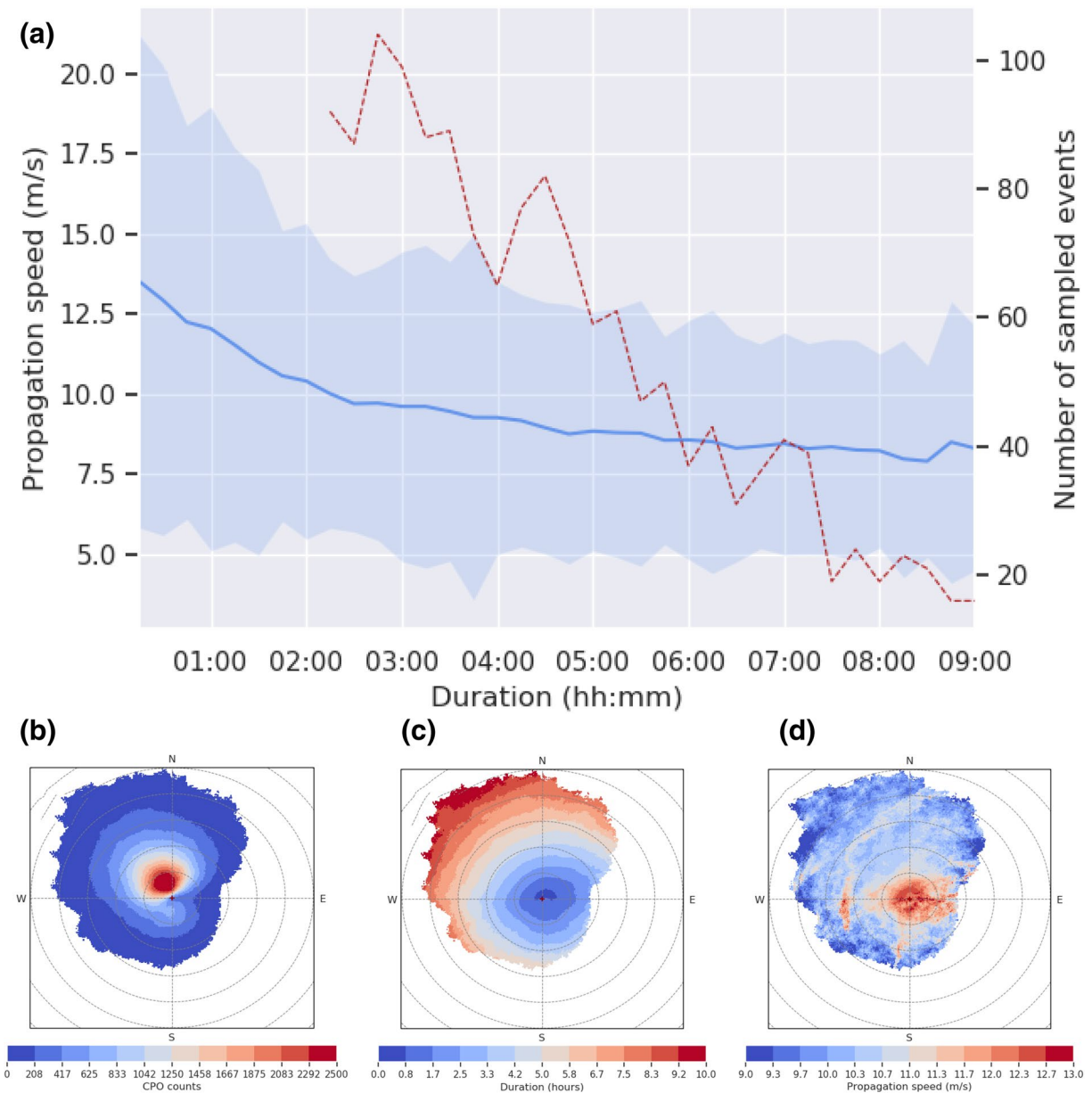


Figure 9. (a) Distribution of CPO durations (red dashed line) with mean propagation speed at that point in the CPO's lifetime (solid blue line, with one standard deviation shaded in light blue). Composites of all CPOs across all timesteps are shown below (b)–(d). Gray dashed concentric circles are spaced at distances of 100 km, with each detected event overlain and centered using its source point (shown as a blue cross in Figure 5). Composites include (b) frequency, (c) mean duration and (d) mean propagation speed. CPO, cold pool outflow.

north along the Mali–Algeria border. CPOs are demonstrably far-reaching in the CWS, with a climatological signal hundreds of kilometers north of the peak WAM rainband. The high occurrence of CPOs in the hyper-arid Sahara confirms that moisture transport pathways exist capable of ventilating the remote SHL region (Engelstaedter et al., 2015) and that CPO recycling may play an important role in sustaining this (Trzeciak et al., 2017) although further work is needed to pinpoint the dominant mechanism by which CPOs are generated this far north of the climatological ITD.

The spatial distribution of CPO hotspots evolves through the summer season. One notable component of this is a northward shift in the band of peak CPO activity, tracing the displacement of the ITD. In June, the maximum in CPO occurrence is found around 18°N in western Mali (with pixels averaging more than one

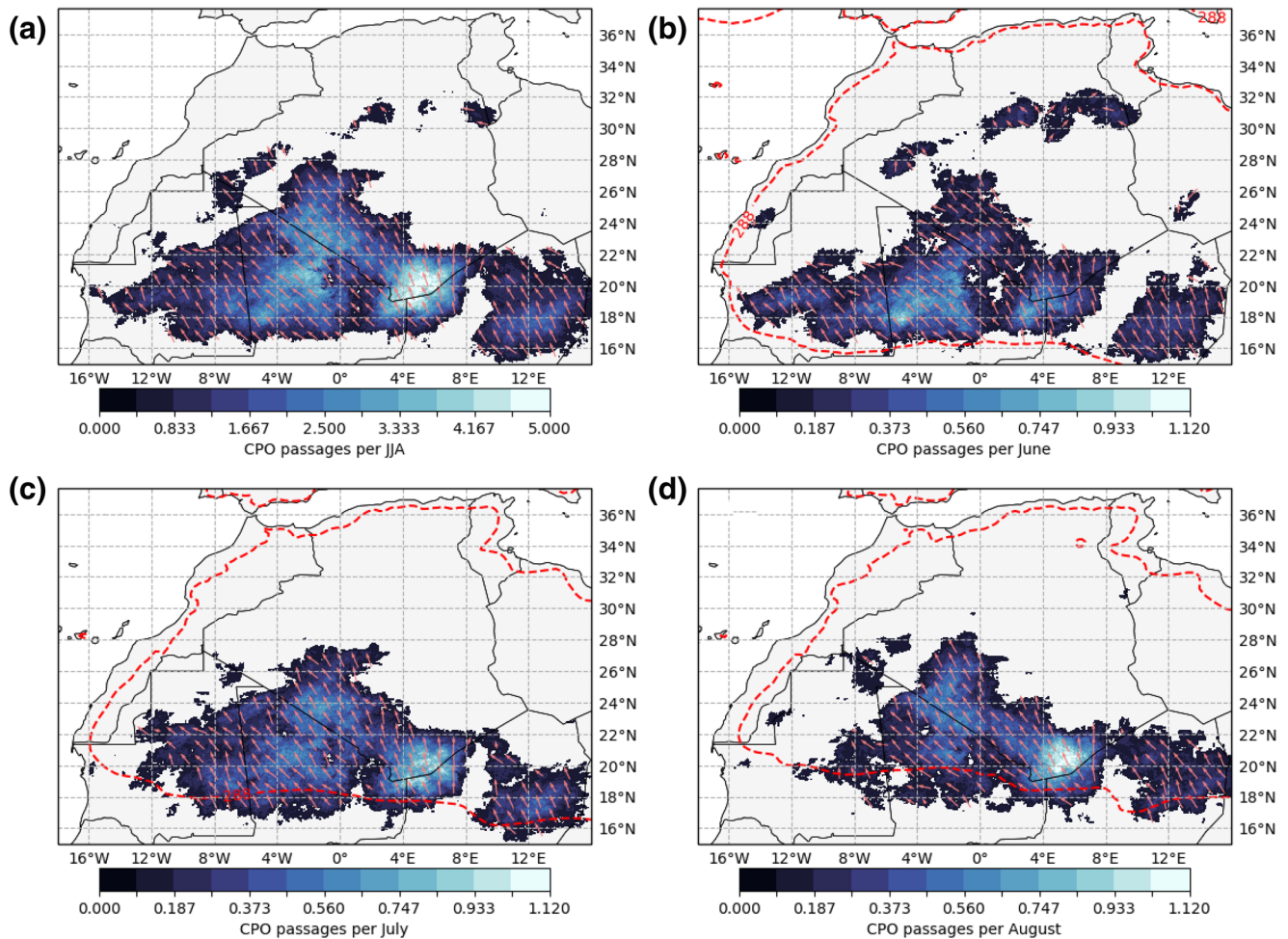


Figure 10. Pixels classified as belonging to CPO events across the total lifetime of all features tracked from 2004 to 2017. Counts per JJA are shown in (a), along with (b) June, (c) July and (d) August. The 270 K 10 m dewpoint temperature line is plotted in red (dashed), of which the southern boundary is a proxy for the ITD position. Pink arrows represent the mean propagation direction of detected events. CPO, cold pool outflow; ITD, intertropical discontinuity.

passage per June) and is mirrored by comparably frequent passages east of the Adrar des Ifoghas mountains at 3°E in the region south of the triple point (Figure 10b). During July, these pixels lose their prominence and a broader distribution of occurrence is observed, including passages north of the Algeria border (24°N) and the development of a CPO hotspot directly north of the triple point (Figure 10c). In August, the southernmost hotspots of occurrence are entirely inactive and the maximum north of the triple point develops to its highest frequency (Figure 10d). Whereas the early monsoon season is associated with a high production of CPOs at Sahelian latitudes, the late season is dominated by activity in the central Sahara. These findings broadly align with modeled dust uplift potential from cold pool outflows calculated for the “Sahara West” domain in Pantillon et al. (2016), where a peak is reached in August (in contrast to an earlier monsoon peak in the Sahel). The patterns are also consistent with maps of CPO-associated dust presence in Caton Harrison et al. (2019) in which a noticeable shift occurs from dust presence in the southern Sahara (including central Mali) toward hotspots further north in southern Algeria in August. However, one important inconsistency between the two datasets is that an intense peak in CPOs in August over the TP in Figure 10d does not appear to map on to the drop in late season dust presence seen in Caton Harrison et al. (2019).

A decline in atmospheric dust loading from the early to late monsoon season is a well-documented feature of the annual cycle of the CWS. It has been noted in SEVIRI dust flags (Ashpole & Washington, 2013a, 2013b; Caton Harrison et al., 2019), MODIS/MISR aerosol optical depth (Ridley et al., 2012; Schepanski

Table 1
Possible Mechanisms for the Late Summer Decline in Saharan Dust Emission

| | Mechanism | Possible drivers |
|---|---|---|
| 1 | Declines in late summer dust emission are an artifact of satellite observing methods | Dust emission obscured by cirrus anvils (Heinold et al., 2013; Redl et al., 2015; Williams, 2008) Masking by increased late-season column water vapor (Brindley et al., 2012) |
| 2 | Decreasing frequency or strength of CPOs drives declines in dust emission during late summer | Lower DCAPE in the late summer season due to decreasing midtropospheric dryness (Marsham et al., 2008; Provod et al., 2016) |
| 3 | Decreasing frequency or strength of nocturnal low-level jets drives declines in dust emission during late summer | Decreased nocturnal boundary layer stability due to the northward advance of the ITD |
| 4 | Key dust sources cease to be collocated with the main meteorological drivers of dust emission during late summer | Less available erodible material in northern/Saharan dust sources as the ITD advances northward |
| 5 | Dust emission remains constant through summer but material is more rapidly deposited or less widely circulated as the season progresses | Increased scavenging of dust due to a late monsoon peak in Saharan rainfall (Engelstaedter & Washington, 2007) |
| 6 | Increased rainfall late in the summer season inhibits dust emission | Limits to wind erosion due to capillary forces within the soil induced by increased moisture content (Bergametti et al., 2016, 2017; Fécan et al., 1998) or crusting (Rajot et al., 2003) |

CPOs, cold pool outflows; ITD, intertropical discontinuity; DCAPE, Downdraft Convective Available Potential Energy.

et al., 2012) and TOMS AI (Engelstaedter & Washington, 2007). Given the importance of CPOs for dust emission, here we compare our CPO data set with observed dust presence through boreal summer.

The relationship between dust emission mechanisms such as CPOs and total dust emission is not straightforward. Table 1 summarizes a number of possible mechanisms responsible for declining late summer Saharan dust emission.

Mechanisms 3, 5 and 6 in Table 1 are not tested directly in this paper, which focuses instead upon CPOs. Peak nocturnal low-level jet occurrence (mechanism 3) is thought to shift northwards through summer (Fiedler et al., 2013) like CPOs. This emission mechanism is secondary to CPOs (Caton Harrison et al., 2019), but may play a complementary role in the overall decline. Differences in dust transport (mechanism 5) are an additional possible factor, but the analysis of Ashpole and Washington (2013b) (Figures 8 therein) clearly flags fewer “dust emission” pixels on average in August compared to June and July. Rainfall (mechanism 6) may also act to inhibit uplift of dust (i.e., decreasing erodibility) in the late monsoon season. This has been explored in some detail for the Sahel by Bergametti et al. (2016, 2017) who find that precipitation inhibits around 25% of dust uplift potential, suggesting only a small role in the late season dust decline. For comparison, rainfall totals (not shown) at Tamanrasset (22.8°N, just north of the apparent August CPO hotspot) reach around 20 mm in August on average, compared to over 140 mm at Tahoua (14.9°N) which is still further north than the field sites used by Bergametti et al. (2017) (e.g., Banizoumbou at 13.5°N). The scarcity of rainfall in the region of the August CPO hotspot therefore casts doubt on the importance of this process, but in situ observations to test for rainfall inhibition over central Saharan dust sources would be extremely valuable.

To test whether the observed dust decline is merely an artifact of satellite observations (mechanism 1), we compare our results to weather observations (in the form of weather codes) from stations reporting data to the Met Office Integrated Data Archive System (MIDAS) within the broader TP region of the CWS. To achieve this, the TP region is split into two domains (Figures 11a): TP-South and TP-North. TP-South represents the region south of the Algerian border for which large declines in dust emission are observed in Ashpole and Washington (2013b) as the dust band shifts north, while TP-North represents the region to the north where dust is observed to be more stable through the summer season but where a CPO hotspot is observed to develop late in the season (Figure 10d).

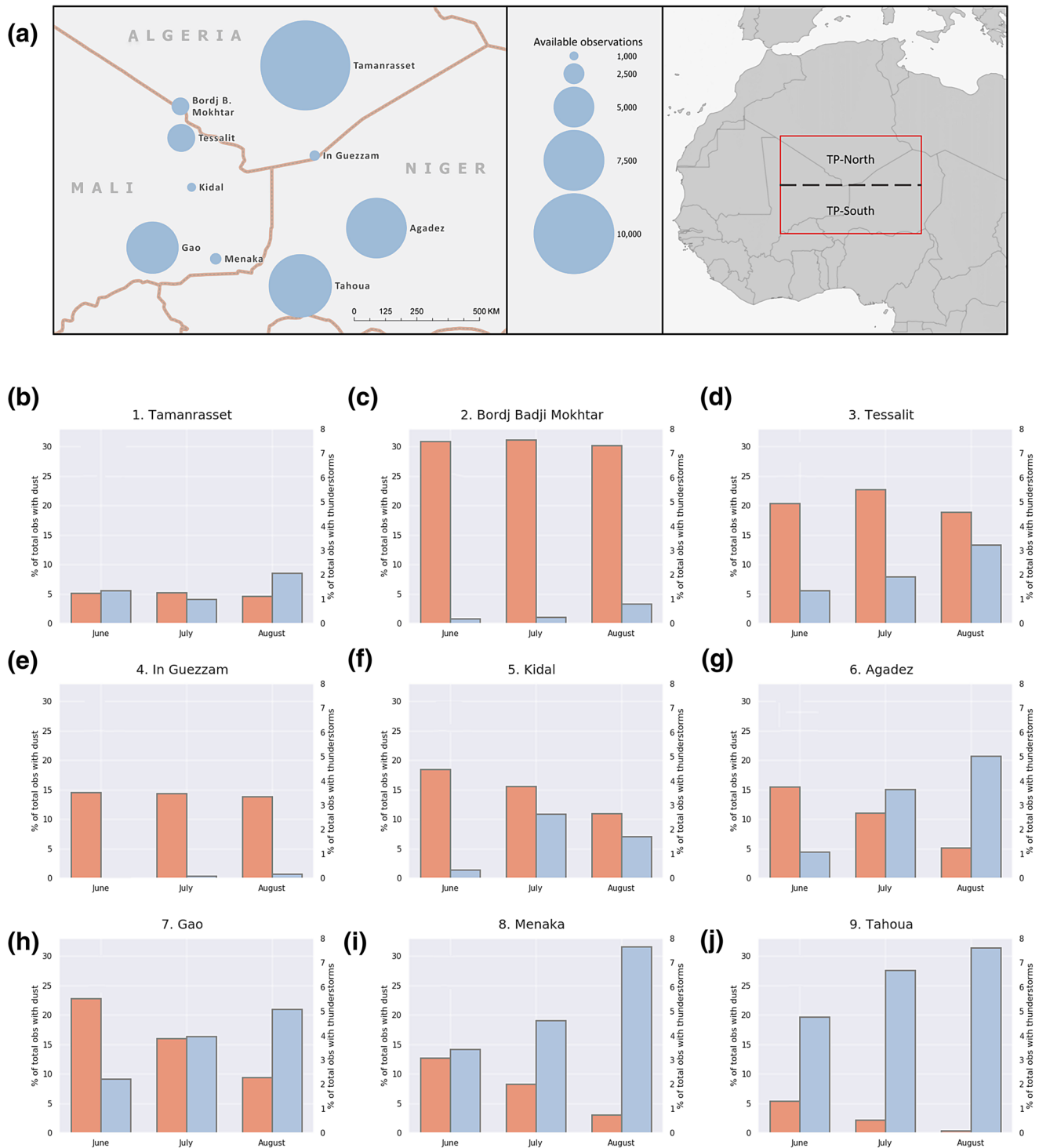


Figure 11. Percentage of observations of weather codes associated with dust activity (orange) and thunderstorms (blue) at stations reporting to the MIDAS for June, July and August. Sampling domain and location of stations is shown in (a) along with the size of circles representing the available samples at each station. The location of the domain as well as the division between TP-North and TP-South are shown in the rightmost panel. Observations are taken from (b) Tamanrasset, (c) Bordj Badji Mokhtar, (d) Tessalit, (e) In Guezzam, (f) Kidal, (g) Agadez, (h) Gao, (i) Menaka and (j) Tahoua. MIDAS, Met Office Integrated Data Archive System; TP, Triple point.

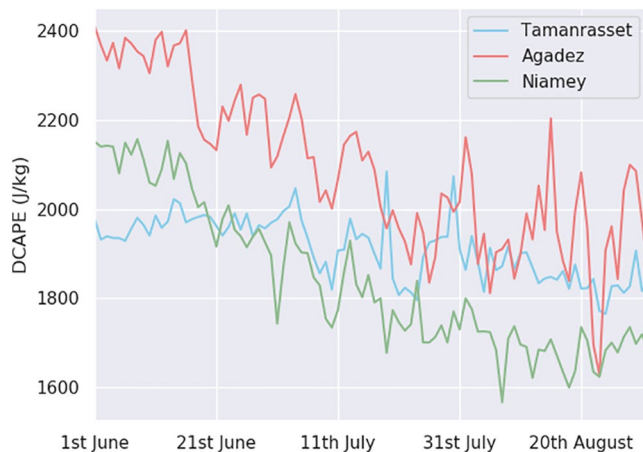


Figure 12. Mean of DCAPE in J/kg measured from sonde ascents at Tamanrasset (blue), Agadez (pink) and Niamey (green) for June, July and August 2004–2017. Daily sonde ascents at 00 and 12 UTC are included in the average. DCAPE is calculated from the level with the lowest wet bulb potential temperature, corresponding to the greatest possible evaporative cooling, following Gilmore and Wicker (1998). DCAPE, Downdraft Convective Available Potential Energy; UTC, Universal Time Coordinated.

et al. [2019]) and CPOs exhibit a clear northward shift in the southern boundary of their occurrence, suggesting that reduced CPO activity south of 20°N is responsible for the drop-off in dust at those latitudes. A possible explanation for this observed decline in the southernmost CPOs is reduced Downdraft Convective Available Potential Energy (DCAPE), as described by Marsham et al. (2008) and Provod et al. (2016). At the peak of the monsoon season, tropical to extratropical moisture transport inhibits dry mid-tropospheric conditions conducive to diabatic cooling and downdraft formation. It should be noted that although it is an important ingredient for cold pool activity, DCAPE alone is generally limited as a predictor of the occurrence and strength of negatively buoyant downdrafts. For example, a parameterization of CPOs based primarily upon DCAPE was found to misplace the peak in CPO activity over the central Sahara at the expense of southern events (Pantillon et al., 2016). DCAPE is shown in Figure 12 for Agadez and Niamey (located in and just south of TP-South, respectively). All available sonde ascents at each of the two stations (red and green lines) are averaged across the period 2004–2017, exhibiting declines of around 500 J/kg through summer. Decreased DCAPE would explain reduced efficiency of CPO production at these latitudes even as thunderstorm activity increases (Figure 11).

Mechanism 2 alone is too simplistic, however, and assumes dust sources are as abundant in TP-North as they are in TP-South. Although declines in CPOs over southern regions are observed in the late summer, a large intense hotspot of CPO occurrence also develops further north during August (Figure 10d). The development of this TP-North hotspot is not paralleled by any major increases in late-season dust observations anywhere in either TP-North or TP-South (Figure 11). Although TP-North does undergo a slight but statistically significant (at the 0.01 level) decrease in DCAPE (Figure 12, blue line), TP-North is located northwest of a major late-season hotspot of deep convective cloud development in the lee of the Air mountains (not shown). This region of preferred convective triggering in August is particularly clearly shown with the microwave satellite imaging method of Redl et al. (2015). Hence, in spite of a general trend of declining DCAPE, large increases in Saharan deep convection around the TP drive a late monsoonal hotspot of southern Algerian CPOs.

Given that CPOs increase in frequency over TP-North during the late summer season, one plausible explanation for reduced dust presence during August is that the CPO hotspot is not collocated with any major dust sources (mechanism 4), and hence that a northward shift in peak CPO activity leads to an overall decline in emission. Although the CPO-tracking algorithm relies on the presence of erodible material to make

The majority of stations within the sampled domain report a decline in the relative frequency of dust-related weather codes in August (Figure 11). In parallel, most stations also report that August is subject to the highest levels of thunderstorm activity, lending credence to the late season CPO hotspot observed in Figure 10d. Dust declines are much larger in TP-South; across the entire sampling period, Tahoua reports only 25 dust observations for the month of August, compared with over 400 in June (Figures 11j). By contrast, counts in Tamanrasset (Figures 11b) and Bordj Badji Mokhtar (Figures 11c) in TP-North are relatively consistent through the summer months, with only a slight decline in August compared to June. A sharper drop in dust activity further south is consistent with Ashpole and Washington (2013b), in which the dust band is observed to shift northward, and implies that this is not merely a result of enhanced cloud cover at these latitudes. These results do not therefore support a hypothesis that dust decreases in August can be explained as a satellite artifact (mechanism 1). There is, however, evidence that the drop in dust is dominated by the seasonality of the southernmost dust sources (mechanism 4).

Mechanism 2 from Table 1 poses that dust emission totals through summer are directly controlled by the frequency of CPOs across the Sahara. Patterns of CPO activity through summer (Figures 10b–10d) suggest that this hypothesis can explain the sharp declines observed in the southernmost dust sources. Both observed dust (e.g. Figure 11 in Caton Harrison

CPOs visible, it is possible that many of the arcs observed in August are linked to dust in shorter supply or coarser material which is immediately redeposited. This suggests that the location of meteorological dust emission mechanisms is just as important as their frequency; as Figure 10 shows, CPO frequency is highly heterogeneous across the Sahara, but for large atmospheric dust loading to occur, they must also be collocated with suitable sources of fine erodible material.

Overall, three important points come out of this analysis. First, several independent datasets show that atmospheric dust loading over the Sahel and Sahara declines in late summer as the ITD moves north and DCAPE declines over the Sahel. Second, manual observations of dust storms decline more rapidly through summer in the TP-South domain than TP-North. Lastly, convective activity and CPOs appear to actually increase over TP-North and the central Sahara during late summer despite no corresponding increase in dust production at these latitudes. Together, these results suggest that the southernmost dust sources play a major role in the summertime dust budget. However, as shown by M. C. Todd and Cavazos-Guerra (2016), dust sources south of 17°N are likely to be underrepresented in the most widely cited Saharan dust source maps (Ashpole & Washington, 2013b; Schepanski et al., 2007). Further in situ observations may also be needed to understand why sharply increasing late-monsoon convective and CPO activity over TP-North has such a minor role in dust production.

5. Summary and Conclusions

Motivated by an absence of observations and reliable model simulations, a 14 years data set of cold pool outflow boundary passage has been derived from high temporal resolution satellite data. To the authors' knowledge, it is the first method for tracking individual dust-laden CPOs through time, and comprises the largest set of Saharan CPO observations in general. It is used here to identify typical CPO characteristics and to analyze the drivers of seasonal trends in Saharan dust activity.

The 10.8–8.7 K Brightness Temperature Difference field from Meteosat SEVIRI data is found to be sensitive to regions where outflow boundaries emit dust and raise local humidity. In order to flag only pixels associated with genuine outflow passages, a multistep algorithm is applied to the data. Regions with a high BTDG in time are highlighted as possible CPO occurrence regions. Thresholds are then applied to the value of the BTDG field, the duration, maximum size reached by individual events and their proximity to deep convection in order to flag genuine CPO pixels. Propagation speed is also estimated for each tracked CPO by fitting events to an idealized 2D model of outflow boundary displacement.

When validated against manually identified CPOs from satellite data for July of 2011, the automated system flags 74.2% of the total events, with only 6.8% of flagged pixels corresponding to false alarms. Of the automatically tracked events which are observable from surface weather station data for 2011 and 2012, a majority leave a clear signal in high resolution wind speed data.

With 1,559 events tracked for June, July and August of 2004–2017, the following findings are made:

- CPO occurrence follows a clear diurnal cycle, peaking at 1700–1900 UTC, consistent with a nocturnal peak in dust emission
- Outflow boundary propagation speeds decay exponentially from the point of CPO generation, peaking overnight (around 1.5 ms^{-1} higher) as vertical mixing is reduced
- Events are overwhelmingly northwestwards propagating, with 351 observed events (22.5%) exceeding 300 km in distance traveled
- CPOs are active across northern Mali, eastern Mauritania, along the western Algerian border and at the triple point of Mali, Niger and Algeria
- The spatial pattern of CPO activity through boreal summer maps onto changes in dust presence, with a northward and eastward shift in CPO occurrence as the monsoon season progresses
- The development of the largest CPO hotspot over the northern triple point region during August does not appear to counteract declines in dust further south, indicating that the southernmost dust sources play a large role in the summertime budget

Saharan CPOs are widespread, diurnally varying, northwestward propagating phenomena which occur further north as the summer season progresses and which peak in frequency to the north of the Mali-Niger-Algeria triple point during August. The results of a comparative analysis of CPO and dust activity suggest that the decline in Saharan dust through summertime is subject to a complex interplay between cold pool outflow activity and the geography of dust availability, with the southernmost sources activated almost exclusively during the early monsoon season. The development of a late-season hotspot of cold pool outflows over southern Algeria does not compensate for this southern decline, indicating that emission within the Sahel is more responsive to varying cold pool activity and may play a pivotal role in the dust budget for the summer season.

Data Availability Statement

Fennec data can be accessed from the Centre for Environmental Data Analysis (<https://catalogue.ceda.ac.uk/uuid/819bdb021a644a9fb0b31704479523db>). MIDAS data are available from CEDA (<https://catalogue.ceda.ac.uk/uuid/0ec59f09b3158829a059fe70b17de951>).

Acknowledgments

MSG SEVIRI data can be accessed online from the EUMETSAT Data Center (<https://navigator.eumetsat.int/product/EO:EUM:DAT:MSG:HRSEVI-RI>). AWS data were collected during the Natural Environment Research Council (NERC) Fennec field campaign (Grant NE/G017166/1). The author would like to thank those who installed and maintained the instrumentation, including the Algerian and Mauritanian Meteorological Offices. T. Caton Harrison is funded through the NERC doctoral training partnership (NE/L002612/1). R. Washington was partly supported by the NERC-Department for International Development (DFID)-funded Improving Model Processes for African Climate (IMPALA) project (Grant NE/M017206/1), as part of the Future Climate for Africa (FCFA) program (<http://futureclimateafrica.org/project/impala/>). The authors are grateful to Ian Ashpole, Neil Hart and three reviewers for insightful discussions and comments which helped improve the manuscript.

References

- Allen, C. J., & Washington, R. (2014). The low-level jet dust emission mechanism in the central Sahara: Observations from Bordj-Badji Mokhtar during the June 2011 fennec intensive observation period. *Journal of Geophysical Research: Atmosphere*, 119(6), 2990–3015.
- Allen, C. J., Washington, R., & Engelstaedter, S. (2013). Dust emission and transport mechanisms in the central Sahara: Fennec ground-based observations from bordj-badji mokhtar, June 2011. *Journal of Geophysical Research*, 118(12), 6212–6232.
- Allen, C. J., Washington, R., & Saci, A. (2015). Dust detection from ground-based observations in the summer global dust maximum: Results from fennec 2011 and 2012 and implications for modeling and field observations. *Journal of Geophysical Research: Atmosphere*, 120(3), 897–916.
- Ashpole, I., & Washington, R. (2012). An automated dust detection using seviri: A multiyear climatology of summertime dustiness in the central and western Sahara. *Journal of Geophysical Research*, 117(D8), 8202.
- Ashpole, I., & Washington, R. (2013). Intraseasonal variability and atmospheric controls on daily dust occurrence frequency over the central and western Sahara during the boreal summer. *Journal of Geophysical Research*, 118(23), 12915–12926.
- Ashpole, I., & Washington, R. (2013). A new high-resolution central and western Saharan summertime dust source map from automated satellite dust plume tracking. *Journal of Geophysical Research*, 118(13), 6981–6995.
- Bachl, F. E., Garbe, C. S., & Fieguth, P. (2012). A Bayesian approach to spaceborn hyperspectral optical flow estimation on dust aerosols. In *Geoscience and remote sensing symposium (IGARSS)* (pp. 256–259). 2012 IEEE International.
- Bagnold, R. A. (1941). *The physics of blown sand and desert dunes*. London, UK: Methuen & Co. LTD.
- Bain, C., Magnusdottir, G., Smyth, P., & Stern, H. (2010). Diurnal cycle of the intertropical convergence zone in the east pacific. *Journal of Geophysical Research*, 115(D23), 361–370.
- Banks, J. R., Schepanski, K., Heinold, B., Hünerbein, A., & Brindley, H. E. (2018). The influence of dust optical properties on the color of simulated msg-SEVIRI desert dust infrared imagery. *Atmospheric Chemistry and Physics*, 18(13), 9681–9703.
- Bedka, K., Brunner, J., Dworak, R., Feltz, W., Otkin, J., & Greenwald, T. (2010). Objective satellite-based detection of overshooting tops using infrared window channel brightness temperature gradients. *Journal of applied meteorology and climatology*, 49(2), 181–202.
- Bedka, K. M., & Khlopenkov, K. (2016). A probabilistic multispectral pattern recognition method for detection of overshooting cloud tops using passive satellite imager observations. *Journal of Applied Meteorology and Climatology*, 55(9), 1983–2005.
- Bergametti, G., Marticorena, B., Rajot, J.-L., Chatenet, B., Féron, A., Gaimoz, C., et al. (2017). Dust uplift potential in the central Sahel: an analysis based on 10 years of meteorological measurements at high temporal resolution. *Journal of Geophysical Research: Atmosphere*, 122(22), 12–433.
- Bergametti, G., Rajot, J. L., Pierre, C., Bouet, C., & Marticorena, B. (2016). How long does precipitation inhibit wind erosion in the Sahel? *Geophysical Research Letters*, 43(12), 6643–6649.
- Bou Karam, D., Flamant, C., Knippertz, P., Reitebuch, O., Pelon, J., Chong, M., & Dabas, A. (2008). Dust emissions over the Sahel associated with the west African monsoon intertropical discontinuity region: A representative case-study. *Quarterly Journal of the Royal Meteorological Society*, 134(632), 621–634.
- Boucher, O., Randall, D., Artaxo, P., Bretherton, C., Feingold, G., Forster, P., et al. (2013). Clouds and aerosols. *Climate change 2013: The physical science basis. Contribution of working group i to the fifth assessment report of the intergovernmental panel on climate change* (pp. 571–657). Cambridge University Press.
- Brindley, H., Knippertz, P., Ryder, C., & Ashpole, I. (2012). A critical evaluation of the ability of the spinning enhanced visible and infrared imager (SEVIRI) thermal infrared red-green-blue rendering to identify dust events: Theoretical analysis. *Journal of Geophysical Research*, 117(D7), 7201.
- Cakmur, R., Miller, R., & Torres, O. (2004). Incorporating the effect of small-scale circulations upon dust emission in an atmospheric general circulation model. *Journal of Geophysical Research*, 109(D7), D07201.
- Caton Harrison, T., Washington, R., & Engelstaedter, S. (2019). A 14-year climatology of Saharan dust emission mechanisms inferred from automatically tracked plumes. *Journal of Geophysical Research: Atmosphere*, 124(16), 9665–9690.
- Cuesta, J., Marsham, J. H., Parker, D. J., & Flamant, C. (2009). Dynamical mechanisms controlling the vertical redistribution of dust and the thermodynamic structure of the west Saharan atmospheric boundary layer during summer. *Atmospheric Science Letters*, 10(1), 34–42.
- Emmel, C., Knippertz, P., & Schulz, O. (2010). Climatology of convective density currents in the southern foothills of the Atlas mountains. *Journal of Geophysical Research*, 115(D11). <https://doi.org/10.1029/2009JD012863>

- Engelstaedter, S., & Washington, R. (2007). Atmospheric controls on the annual cycle of north African dust. *Journal of Geophysical Research*, *112*(D3). <https://doi.org/10.1029/2006JD007195>
- Engelstaedter, S., Washington, R., Flamant, C., Parker, D. J., Allen, C., & Todd, M. (2015). The Saharan heat low and moisture transport pathways in the central Sahara – Multi-aircraft observations and Africa-Lam evaluation. *Journal of Geophysical Research: Atmosphere*, *120*(10), 4417–4442.
- Engerer, N. A., Stensrud, D. J., & Coniglio, M. C. (2008). Surface characteristics of observed cold pools. *Monthly Weather Review*, *136*(12), 4839–4849.
- Fécan, F., Marticorena, B., & Bergametti, G. (1998). Parametrization of the increase of the Aeolian erosion threshold wind friction velocity due to soil moisture for arid and semi-arid areas. *Annales Geophysicae*, *17*, 149–157.
- Fiedler, S., Schepanski, K., Heinold, B., Knippertz, P., & Tegen, I. (2013). Climatology of nocturnal low-level jets over north Africa and implications for modeling mineral dust emission. *Journal of Geophysical Research*, *118*(12), 6100–6121.
- Flamant, C., Chaboureaud, J.-P., Parker, D., Taylor, C., Cammas, J.-P., Bock, O., & Pelon, J. (2007). Airborne observations of the impact of a convective system on the planetary boundary layer thermodynamics and aerosol distribution in the inter-tropical discontinuity region of the west African monsoon. *Quarterly Journal of the Royal Meteorological Society*, *133*(626), 1175–1189.
- Flamant, C., Knippertz, P., Parker, D. J., Chaboureaud, J. P., Lavaysse, C., Agusti-Panareda, A., & Kergoat, L. (2009). The impact of a mesoscale convective system cold pool on the northward propagation of the intertropical discontinuity over west Africa. *Quarterly Journal of the Royal Meteorological Society*, *135*(638), 139–159.
- García-Carreras, L., Marsham, J., Parker, D., Bain, C., Milton, S., Saci, A., & Washington, R. (2013). The impact of convective cold pool outflows on model biases in the Sahara. *Geophysical Research Letters*, *40*(8), 1647–1652.
- Gilmore, M. S., & Wicker, L. J. (1998). The influence of mid-tropospheric dryness on supercell morphology and evolution. *Monthly Weather Review*, *126*(4), 943–958.
- Grogan, D. F., & Thorncroft, C. D. (2019). The characteristics of African easterly waves coupled to Saharan mineral dust aerosols. *Quarterly Journal of the Royal Meteorological Society*, *145*(720), 1130–1146.
- Heinold, B., Knippertz, P., Marsham, J., Fiedler, S., Dixon, N., Schepanski, K., & Tegen, I. (2013). The role of deep convection and nocturnal low-level jets for dust emission in summertime west Africa: Estimates from convection-permitting simulations. *Journal of Geophysical Research*, *118*(10), 4385–4400.
- Hersbach, H., & Dee, D. (2016). Era5 reanalysis is in production. *ECMWF Newsletter*, *147*(7), 5–6.
- Hirose, M., Oki, R., Shimizu, S., Kachi, M., & Higashiuwatoko, T. (2008). Finescale diurnal rainfall statistics refined from eight years of TRMM PR data. *Journal of Applied Meteorology and Climatology*, *47*(2), 544–561.
- Hobby, M., Gascoyne, M., Marsham, J. H., Bart, M., Allen, C., Engelstaedter, S., & others (2013). The fennec automatic weather station (AWS) network: Monitoring the Saharan climate system. *Journal of Atmospheric and Oceanic Technology*, *30*(4), 709–724.
- Holmes, J. D., & Oliver, S. (2000). An empirical model of a downburst. *Engineering Structures*, *22*(9), 1167–1172.
- Karam, D. B., Williams, E., Janiga, M., Flamant, C., McGraw-Herdig, M., Cuesta, J., & Thorncroft, C. (2014). Synoptic-scale dust emissions over the Sahara Desert initiated by a moist convective cold pool in early august 2006. *Quarterly Journal of the Royal Meteorological Society*, *140*(685), 2591–2607.
- Knippertz, P., Deutscher, C., Kandler, K., Müller, T., Schulz, O., & Schütz, L. (2007). Dust mobilization due to density currents in the atlas region: Observations from the Saharan mineral dust experiment 2006 field campaign. *Journal of Geophysical Research*, *112*(D21).
- Knippertz, P., & Fink, A. H. (2006). Synoptic and dynamic aspects of an extreme springtime Saharan dust outbreak. *Quarterly Journal of the Royal Meteorological Society*, *132*(617), 1153–1177.
- Knippertz, P., & Todd, M. C. (2010). The central west Saharan dust hot spot and its relation to African easterly waves and extratropical disturbances. *Journal of Geophysical Research*, *115*(D12).
- Knippertz, P., & Todd, M. C. (2012). Mineral dust aerosols over the Sahara: Meteorological controls on emission and transport and implications for modeling. *Reviews of Geophysics*, *50*(1).
- Kocha, C., Tulet, P., Lafore, J.-P., & Flamant, C. (2013). The importance of the diurnal cycle of aerosol optical depth in west Africa. *Geophysical Research Letters*, *40*(4), 785–790.
- Lavaysse, C., Flamant, C., Janicot, S., Parker, D., Lafore, J.-P., Sultan, B., & Pelon, J. (2009). Seasonal evolution of the west African heat low: a climatological perspective. *Climate Dynamics*, *33*(2–3), 313–330.
- Liu, C., Fieguth, P., & Garbe, C. (2012). Background subtraction and dust storm detection. *Geoscience and remote sensing symposium (IGARSS)* (pp. 2179–2181). 2012 IEEE International.
- Lunt, D., & Valdes, P. (2002). The modern dust cycle: Comparison of model results with observations and study of sensitivities. *Journal of Geophysical Research*, *107*(D23), AAC–1.
- Mahowald, N. M., Kloster, S., Engelstaedter, S., Moore, J. K., Mukhopadhyay, S., McConnell, J. R., & others (2010). Observed 20th century desert dust variability: Impact on climate and biogeochemistry. *Atmospheric Chemistry and Physics*, *10*(22), 10875–10893.
- Marsham, J. H., Dixon, N. S., Garcia-Carreras, L., Lister, G. M., Parker, D. J., Knippertz, P., & Birch, C. E. (2013). The role of moist convection in the west African monsoon system: Insights from continental-scale convection-permitting simulations. *Geophysical Research Letters*, *40*(9), 1843–1849.
- Marsham, J. H., Knippertz, P., Dixon, N. S., Parker, D. J., & Lister, G. (2011). The importance of the representation of deep convection for modeled dust-generating winds over west Africa during summer. *Geophysical Research Letters*, *38*(16). <https://doi.org/10.1029/2011GL048368>
- Marsham, J. H., Parker, D. J., Grams, C. M., Taylor, C. M., & Haywood, J. M. (2008). Uplift of Saharan dust south of the intertropical discontinuity. *Journal of Geophysical Research*, *113*(D21). <https://doi.org/10.1029/2008JD009844>
- Marsham, J. H., Parker, D. J., Todd, M. C., Banks, J. R., Brindley, H. E., Garcia-Carreras, L., & Ryder, C. L. (2016). The contrasting roles of water and dust in controlling daily variations in radiative heating of the summertime Saharan heat low. *Atmospheric Chemistry and Physics*, *16*(5), 3563–3575.
- Murray, J. E., Brindley, H. E., Bryant, R. G., Russell, J. E., Jenkins, K. F., & Washington, R. (2016). Enhancing weak transient signals in SEVIRI false color imagery: Application to dust source detection in southern Africa. *Journal of Geophysical Research: Atmosphere*, *121*(17), 10199–10219.
- Pantillon, F., Knippertz, P., Marsham, J. H., & Birch, C. E. (2015). A parameterization of convective dust storms for models with mass-flux convection schemes. *Journal of the Atmospheric Sciences*, *72*(6), 2545–2561.
- Pantillon, F., Knippertz, P., Marsham, J. H., Panitz, H.-J., & Bischoff-Gauss, I. (2016). Modeling haboob dust storms in large-scale weather and climate models. *Journal of Geophysical Research: Atmosphere*, *121*(5), 2090–2109.
- Parker, D. J. (1996). Cold pools in shear. *Quarterly Journal of the Royal Meteorological Society*, *122*(535), 1655–1674.

- Parker, D., Burton, R., Diongue-Niang, A., Ellis, R., Felton, M., Taylor, C., & Tompkins, A. (2005). The diurnal cycle of the west African monsoon circulation. *Quarterly Journal of the Royal Meteorological Society*, *131*(611), 2839–2860.
- Pope, R., Marsham, J., Knippertz, P., Brooks, M., & Roberts, A. (2016). Identifying errors in dust models from data assimilation. *Geophysical Research Letters*, *43*(17), 9270–9279.
- Prospero, J. M., & Lamb, P. J. (2003). African droughts and dust transport to the Caribbean: Climate change implications. *Science*, *302*(5647), 1024–1027.
- Provod, M., Marsham, J., Parker, D., & Birch, C. (2016). A characterization of cold pools in the west African Sahel. *Monthly Weather Review*, *144*(5), 1923–1934.
- Rajot, J., Alfaro, S., Gomes, L., & Gaudichet, A. (2003). Soil crusting on sandy soils and its influence on wind erosion. *Catena*, *53*(1), 1–16.
- Redl, R., Fink, A. H., & Knippertz, P. (2015). An objective detection method for convective cold pool events and its application to northern Africa. *Monthly Weather Review*, *143*(12), 5055–5072.
- Redl, R., Knippertz, P., & Fink, A. H. (2016). Weakening and moistening of the summertime Saharan heat low through convective cold pools from the Atlas mountains. *Journal of Geophysical Research: Atmosphere*, *121*(8), 3907–3928.
- Ridley, D., Heald, C., & Ford, B. (2012). North African dust export and deposition: A satellite and model perspective. *Journal of Geophysical Research*, *117*(D2), D02202.
- Roberts, A., & Knippertz, P. (2012). Haboobs: convectively generated dust storms in west Africa. *Weather*, *67*(12), 311–316.
- Roberts, A., & Knippertz, P. (2014). The formation of a large summertime Saharan dust plume: Convective and synoptic-scale analysis. *Journal of Geophysical Research: Atmosphere*, *119*(4), 1766–1785.
- Roberts, A. J., Woodage, M. J., Marsham, J. H., Highwood, E. J., Ryder, C. L., McGinty, W., & Crook, J. (2018). Can explicit convection improve modeled dust in summertime west Africa?. *Atmospheric Chemistry and Physics*, *18*(12), 9025–9048.
- Ryder, C., McQuaid, J., Flamant, C., Rosenberg, P., Washington, R., Brindley, H., & others (2015). Advances in understanding mineral dust and boundary layer processes over the Sahara from fennec aircraft observations. *Atmospheric Chemistry and Physics*, *15*(14), 8479–8520.
- Schepanski, K., Tegen, I., Laurent, B., Heinold, B., & Macke, A. (2007). A new Saharan dust source activation frequency map derived from MSG-SEVIRI IR-channels. *Geophysical Research Letters*, *34*(18), L18803-L18803-5.
- Schepanski, K., Tegen, I., & Macke, A. (2012). Comparison of satellite based observations of Saharan dust source areas. *Remote Sensing of Environment*, *123*, 90–97.
- Sodemann, H., Lai, T., Marengo, F., Ryder, C. L., Flamant, C., Knippertz, P., & McQuaid, J. B. (2015). Lagrangian dust model simulations for a case of moist convective dust emission and transport in the western Sahara region during fennec/ladunex. *Journal of Geophysical Research: Atmosphere*, *120*(12), 6117–6144.
- Sutton, L. (1925). Haboobs. *Quarterly Journal of the Royal Meteorological Society*, *51*(213), 25–30.
- Tegen, I., Schepanski, K., & Heinold, B. (2013). Comparing two years of Saharan dust source activation obtained by regional modeling and satellite observations. *Atmospheric Chemistry and Physics*, *13*(5), 2381–2390.
- Thorncroft, C., & Blackburn, M. (1999). Maintenance of the African easterly jet. *Quarterly Journal of the Royal Meteorological Society*, *125*(555), 763–786.
- Todd, M., Allen, C. T., Bart, M., Bechir, M., Bentoufouet, J., Brooks, B., & others (2013). Meteorological and dust aerosol conditions over the western Saharan region observed at fennec supersite-2 during the intensive observation period in June 2011. *Journal of Geophysical Research*, *118*(15), 8426–8447.
- Todd, M. C., & Cavazos-Guerra, C. (2016). Dust aerosol emission over the Sahara during summertime from cloud-aerosol lidar with orthogonal polarization (CALIOP) observations. *Atmospheric Environment*, *128*, 147–157.
- Trzeciak, T. M., Garcia-Carreras, L., & Marsham, J. H. (2017). Cross-Saharan transport of water vapor via recycled cold pool outflows from moist convection. *Geophysical Research Letters*, *44*(3), 1554–1563.
- Vizy, E. K., & Cook, K. H. (2009). A mechanism for African monsoon breaks: Mediterranean cold air surges. *Journal of Geophysical Research*, *114*(D1).
- Wagner, R., Schepanski, K., Heinold, B., & Tegen, I. (2016). Interannual variability in the Saharan dust source activation – Toward understanding the differences between 2007 and 2008. *Journal of Geophysical Research: Atmosphere*, *121*(9), 4538–4562.
- Washington, R., Todd, M., Middleton, N. J., & Goudie, A. S. (2003). Dust-storm source areas determined by the total ozone monitoring spectrometer and surface observations. *Annals of the Association of American Geographers*, *93*(2), 297–313.
- Williams, E. (2008). Comment on “atmospheric controls on the annual cycle of north African dust” by S. Engelstaedter and R. Washington. *Journal of Geophysical Research*, *113*(D23), D03103.